Manipulation of stimulus waveform and frequency permits targeted fiber activation during vagus nerve stimulation in 2 rodent species

Yao-Chuan Chang[1, *], Umair Ahmed[1], Naveen Jayaprakash[1], Adam Abbas[1], Qihang Lin[2], Ibrahim Mughrubi[1], Tianruo Guo[2], Yi-Chen Wu[1], Arielle H. Gabalski[1], Anna Daytz[1], Jason Ashville[1], Dokos Socrates[2], Yousef Al-Abed[1], Stavros Zanos[1, *]

[1] Institute of Bioelectronic Medicine, Feinstein Institutes for Medical Research, Manhasset NY 11030, United States

[2] Graduate School of Biomedical Engineering, University of New South Wales, Sydney, 2052, Australia

[*] Corresponding authors: Yao-Chuan Chang and Stavros Zanos

Abstract

Cervical vagus nerve stimulation (VNS) provides relatively minimally-invasive access to vagal fiber populations innervating most visceral organs, making it an attractive therapy candidate for various diseases. To maximize desired and minimize off-target effects, VNS should be delivered in a fiber-selective manner. We sought to select and optimize parameters that preferentially activate large, intermediate or small-size vagal fibers in 2 animal species, rats and mice. We manipulated stimulus waveform and frequency of short-duration (10-s) stimulus trains (SSTs) at different intensities and measured fiber-specific stimulus-elicited compound action potentials, corresponding cardiorespiratory vagally-mediated responses and neuronal expression of c-FOS in sensory and motor brainstem nuclei. We compiled selectivity indices from those measurements to determine optimal parameters for each fiber type. Large- and intermediate-size fibers are activated by SSTs of 30 Hz frequency, using short-square and long-square or quasi-trapezoidal pulses, respectively, at different optimal intensities for different animals. Small-size fibers are activated by SSTs of frequencies >8KH at high stimulus intensities; using a computational model of vagal fibers we find that sodium channels may underlie this effect. All findings were consistent between rats and mice. Our study provides a robust design and optimization framework for targeting vagal fiber populations for improved safety and efficacy of VNS therapies.

Introduction

The vagus nerve has been regarded as a desired target for neuromodulation therapies as it extensively innervates visceral organs and relays information between tremendous number of peripheral receptors, effector cells, and the brain[1]. Cervical vagus nerve stimulation (cVNS),

with its accessibility[2], has been successfully applied to clinical models in drug-resistant epilepsy[3], depression[4], and rheumatoid arthritis[5], and tested in lots of pre-clinical applications including Alzheimer's disease[6], pain[7], anxiety[8], tinnitus[9], heart failure[10], diabetes[11] obesity[12], and pulmonary hypertension[13]. The therapeutic actions of cVNS, though still under investigation, are believed to be mediated by activation of different types of fibers within VN. For example, anti-epileptic action is thought to be related to afferent, large, myelinated A-fibers[14], cardio-inhibitory action in heart failure to efferent, medium, myelinated B fibers[15], and anti-inflammatory action by B- and possible by afferent, small, unmyelinated C-fiber[16,17]. To develop safe and effective VNS protocols for existing and future indications, optimization of stimulation strategies to achieve fiber-selective and function-specific neuromodulation is essential.

One of major challenges of VNS, as well for other peripheral nerve stimulation applications, is the inverse electrical recruitment order of large-to-small diameter fibers. As a result, some of the off-target effects of cervical VNS, such as the activation of efferent A-fibers innervating laryngeal and pharyngeal muscles, often limit the therapeutic efficacy[18-21]. Several stimulation strategies have been used to reverse the fiber recruitment order. Anodal block is a well-documented technique that has been used to suppress the A-fiber associated response or bias the afferent/efferent pathway of the VN[22,23]. Through hyperpolarization of the nerve fiber near an anode, the action potential is biased toward the opposite direction. As the larger fibers are more sensitive to hyperpolarizing current, the threshold for larger fiber to achieve the anodal block is less than smaller fibers. However, for anodal block, the control of proper stimulus intensity the critical so it's difficult to accomplish perfect directional activation as the random distribution of nerve fiber within the predominantly unifascicular cervical VN.

Waveform manipulation, in addition to the anodal block, is the other technique used to for differential nerve stimulation, including slowly rising (or triangular) pulses[22,24,25], pre-pulse[22], and quasi-trapezoidal (QT) (or exponential falling)[22,26]. The mechanism for a slowly-rising pulse can be attributed to different spatial distribution of the ion channels for large and small nerve fibers, as the distant nodes of Ranvier of larger fiber are hyperpolarized more than distant node of smaller fibers; however the adequate pulse duration and slope is important to achieve good selectivity[27]. For a depolarizing prepulse, the nerve fiber is first conditioned with subthreshold current, resulting in inactivation of the voltage dependent sodium channel and increase of excitation threshold[28,29]. Such type of pulse has limitation originated from the unique waveform, as the prolonged phase leads to high charge injection and limit the stimulation frequency. The QT pulse is designed to depolarizing the nerve under cathode and simultaneous selective blockade under anode[30], and has been validated theoretically and experimentally in an functional implanted devices[31]. In large animal experiment, the QT pulse has been shown with promising effect on VNS to prevent laryngeal spasm[26].

High frequency stimulation, also called KHz-range electrical stimulation (KES), used frequently alternating (>1-KHz) rectangular or sinusoidal current to block the neural conduction in peripheral axons[28], and most early studies tested with somatic nerve while monitoring the large efferent fiber response and related muscle force[28,32]. Recently, KES has been applied to VN to regulate anti-inflammatory effect[32], satiety and appetite[33,34], and through electrophysiological study, the KES resulted block effect is not limited to larger fibers but all fiber types, and response are recoverable with proper stimulation dose range and rest time[35]. The actual mechanism behind the KES is still under huge debate, but most likely related to the dynamics of the sodium channel[13,36].

In this study, we leverage both waveform and frequency modulation stimulation strategies to achieve selective VN activation for different fiber types, and validated the results through evoked compound action potentials (eCAPs) recordings and corresponding physiological effects, including laryngeal electromyography (EMG), heart rate (HR) changes and breathing rate (BR) changes. A new concept of neural selective index and physiological selective index has been proposed to optimize the stimulation protocol through maximizing the desire and minimizing the side effect, and the results are consistent with each other. We found the A- and B-fiber selective activation can be attained through waveform manipulation with low pulsing frequency, thought the optimal intensity range varies across animals. Through KES with special design of combined stimulation protocol with probing pulse, the selective C-fiber activation is validated through both neural and physiological responses. We further used a computational model of myelinated and un-myelinated nerve fibers to simulate how different fibers response to the KES and the possible mechanism behind the selective activation. Finally, we performed histology study in brainstem to confirm that the KES can increase the selective ratio of sensory neurons over motor neurons compared with low frequency stimuli (30Hz). The results support the future VNS therapy design that potentially forms more effective fiber-selective, function-specific modulation with minimized off-target effect.

Methods

Animal preparation, anesthesia, physiological instrumentation

Forty-two adult male Sprague Dawley rats (age 2-5 months and weight between 300-550 gm) and eleven male C57BL/6 mice (2-4 months and weight between 25-30 gm) were used in the study under the approval of the Institutional Animal Care and Use Committee at The Feinstein Institutes for Medical Research. Rodents were anaesthetized using isoflurane (induction at 4% and maintenance at 1.5-2%) and medical oxygen; anesthesia was maintained throughout the experiment. Body temperature was measured with a rectal probe and maintained between 36.5-37.5°C using a heating pad (78914731, Patterson Scientific) connected to a warm water recirculator (TP-700 T, Stryker). ECG was recorded by using 3-lead needle electrodes subcutaneously on the limbs and amplified using a commercial octal bio-amplifier (FE238, ADI). Breathing was monitored by using a temperature probe placed outside of the nostrils along with a bridge amplifier (FE221, ADI); the probe reported changes in air temperature during breathing movements: drop in temperature during inhalation, and rise during exhalation (Fig. S1A and B). All physiological signals were first digitized and then acquired at 1-KHz (PowerLab 16/35, ADI) and visualized on LabChart v8 (all from ADInstruments Inc).

Surgical preparation and vagus electrode placement

To expose the cervical vagus nerve (cVN) in the rat model, a midline 3 cm skin incision was given on the neck (Fig. S1A). Salivary glands were separated, and muscles were retracted to reach the carotid bundle. Under a dissecting microscope, the right cVN was isolated first at the caudal end of nerve and then at rostral end of nerve. The middle portion, between the two isolated sites was left intact within carotid bundle to minimize the extent of surgical manipulation and trauma to the nerve. After isolation of the nerve, a pair of custom-made, tripolar cuff electrodes was placed on the caudal and rostral sites relative to omohyoid muscle (Fig. S1A). The cuff electrodes were made use a polyimide substrate and sputter-deposited iridium oxide contacts for low electrode impedances and stable stimulation characteristics[37-39]. Electrode contacts had dimensions of 1418×167 μm^2 with an edge-to-edge spacing of 728 µm and center-to-center spacing of 895 µm. Typical individual electrode impedances in saline ranged from 0.5 to 1.5 kΩ. The distance between the stimulating electrode (center contact of

tripolar cuff) to the most proximal recording electrode on the nerve was measured roughly 5 to 6 mm. Silicone elastomer (Kwiksil by World Precision Instruments) was placed around the cuff to minimize current leakage during stimulation. In the mouse model, all surgical procedures were identical except the left cVN was targeted. In addition, for direct laryngeal muscle measurement, the thyroid cartilage was exposed by separating the sternohyoid muscle at the midline using blunt dissection. Using a 29G insulin syringe, a shallow slit was made in the thyroid cartilage just lateral and inferior to the laryngeal prominence. With the needle bevel facing up, the two PTFE-coated platinum-iridium wires were carefully inserted into the underlying laryngeal muscles through the slit guided by the syringe needle.

Vagus nerve recording and stimulation

Neural activity from each contact on the recording electrode was amplified, digitized (30KS/s, 16bit resolution) and filtered (60-Hz notch), using a 32-channel RHS2000 stim/record headstage and 128ch Stimulation/Recording controller (Intan Technologies); recordings were single-ended, relative to a ground lead placed in the salivary gland. Nerve stimulation was delivered in constant current mode as trains of pulses using an STG4008 stimulus generator (Multichannel Systems). For all experiment related to waveform manipulation, the stimulation protocols were composed of monophasic pulse with varying pulse width, intensity, polarity, and waveform shape. Monophasic pulses were used here to yield lower threshold and simpler stimulus artifact shape. Even though pulses were not charge-balanced, it is unlikely that during these acute experiments with low pulsing frequency, significant charge build-up occurred. In particular, fully randomized single pulse with 30-s on and 10-s off at 1Hz were used to access the neural response, whereas stimulus trains of 10-s durations with identical type of pulse at 30Hz were randomly delivered to evoked discernable physiological response. For experiment related to frequency manipulation, all the stimuli were delivered in biphasic form except for probing pulse, to maintain the charge balancing across the neural interface and minimize the neural injury. All the stimuli were constructed as train form with consistent 10-s duration but with varying frequency, pulse width, and intensity, and randomly delivered from a range. The stimulation configuration was tripolar (cathode-center or cathode-corner) as it outperforms in terms of protection of current leakage for all experiments. There were at least 15-s long pauses between successive trains to ensure that physiological measurements had reached a steady state before a new train was delivered.

In all experiments with neural recording, we initially determined the “neural threshold” (NT) as the lowest stimulus intensity for a 100-µs duration pulses that evoked a discernable evoked potential at the recording electrode. The physiological threshold (PT), which evoked visible (5-10%) heart rate/respiratory change (usually 3 or 4×NT), was used in experiment when no neural signals were recorded and for all KES experiments. The details of each experiment can be found in Table S1 and S2.

Specifically, to access the neural activity in response to the KES with one stimulation cuff, we designed the waveform, which is combined with KES with low frequency, 1Hz probing pulse, as the low frequency probing pulse does not contribute significantly to physiological effect[40]. For each probing pulse, a 30-ms window (5ms before, 25ms after the onset) is opened in the 10-s KES train, to improve the signal-to-noise ratio for further evoked neural signal processing in next section.

Identification and analysis of neural and EMG signals

Raw nerve signal traces from both electrodes were filtered using a 1Hz high-pass filter to remove the DC component. Stimulus-evoked compound action potentials (eCAPs) elicited from individual pulses or from trains of pulses, were extracted, by averaging individual sweeps of nerve recording traces around the onset of pulses (waveform manipulation experiments) or

probing pulse (frequency manipulation experiments). A custom-made buffer amplifier was used to record the induced voltage on the electrode during stimulation. Stimulation artifact was suppressed offline for waveform manipulation experiment by a recently proposed method which subtracts the trace of the stimulation electrode voltage from the eCAPs with proper template matching and an edge effect removal algorithm[41]. For frequency manipulation, due to the saturation of artifact voltage buffer, same artifact removal algorithm has not been applied. Given the rough estimation of distance between the recording and stimulation electrodes (5-6 mm), we fine tune the distance in analysis so that the latency windows can align well with the A-, B- and C-fiber prominent peaks with pre-defined conduction velocity ranges for each fiber type (A: 5-120 m/s; B: 2-8 m/s; C: 0.1-0.8 m/s)[42]. Fig. S1C shows representative eCAP, including activity of different fiber types and EMG. Signals from both contacts in the recording electrode, proximal and distal to the stimulating electrode, were collected (solid blue and dashed red traces in Fig. S1C). This allowed to distinguish between neural and EMG signal components. For the given electrode spacing A- and B-fibers had short latencies (< 3 ms, red and green windows), while slower C-fibers occurred at longer latencies (> 6 ms, yellow window)[41]. To discriminate C-fiber components from EMG, we reasoned that C-fiber volleys should show a latency difference between the proximal and distal recording contact, spaced apart by a distance of 895 μm, of 1-2 ms, whereas EMG signals should occur simultaneously on both recording contacts[41] (Fig. S1C, grey window), with time window around 2-6ms (identified with neuromuscular junction blocking agent in our previous study[40]).

Analysis of physiological signals

We computed the magnitude of EMG response from respective eCAPs as the peak-to-trough amplitude of the (typically biphasic) response within the EMG window (Fig. S1C, grey window).; that amplitude was then normalized by the maximum EMG amplitude in that subject. Using a custom algorithm, ECG peaks corresponding to the R waves were identified, and heart rate (HR) was computed from R-R intervals. We defined stimulus-induced change in HR (ΔHR) as the difference between the mean HR during a 10-s epoch before the onset of the stimulus train ("Before-VNS") and the mean HR during the stimulus train ("During-VNS"), divided the mean pre-stimulus HR. In recordings from the nasal temperature sensor, we identified peaks (end of expiration) and troughs (end of inspiration). We defined the interval between two successive peaks (or two successive troughs) as breathing interval (BI). We defined the stimulus-elicited change in breathing interval (ΔBI) as the difference between the mean pre-stimulus and the mean during-stimulus BI. For those cases without breath during stimulation period, the breathing interval between last breath of pre-stimulus and first breath post-stimulus was used as mean during-stimulus BI. The measured signals and corresponding derived variables (ECG and ΔHR, and nasal sensor temperature and ΔBI) are shown in Fig. S1B. All the analyses were performed using MATLAB 2016a software (MathWorks, Natik, MA, USA).

Physiological and neural selective indices

To evaluate the fiber selective performance of tested stimulation parameters, for different types of fibers, we have defined neural selective indices (NSIs) which aim to maximize target and minimize off-target fiber activity. The NSIs for A-, B-, C-fibers are:

$$NSI(A-fiber) = \frac{A}{B+C+\varepsilon}$$

$$NSI(B-fiber) = \frac{B}{A+C+\varepsilon}$$

$$NSI(C-fiber) = \frac{C}{A+B+\varepsilon}$$

where *A*, *B*, *C* are normalized evoked fiber activity within each animal, and a small constant ε is used to prevent the overflow due to the extremely small fiber activity in the denominator.
Similar to NSIs, based on an existing relationship/models between fiber activity and physiological response: A-fiber to evoked EMG, B-fiber to HR, and C-fiber to BI (Fig. S2), we further defined physiological selective indices (PSIs) which aim to maximize desired and minimized non-desired physiological effects corresponding to different type of fiber activation. The PSI for A-, B-, C-fibers defined as:

$$PSI(A-fiber) = \frac{EMG(norm.)}{\Delta HR(norm.) + \Delta BI(norm.) + \varepsilon}$$

$$PSI(B-fiber) = \frac{\Delta HR(norm.)}{EMG(norm.) + \Delta BI(norm.) + \varepsilon}$$

$$PSI(C-fiber) = \frac{\Delta BI(norm.)}{EMG(norm.) + \Delta HR(norm.) + \varepsilon}$$

where *EMG(norm.)*, *ΔHR(norm.)*, and *ΔBI(norm.)* are normalized physiological responses within each animal, and a small constant ε is used to prevent the overflow, same as NSI. To quantify the performance of PSIs using different stimulation parameters across animals, a 1st order Gaussian model was computed to capture the relationship between computed PSIs and different stimulation intensities.

Immunohistochemistry

Rats were deeply anesthetized with isoflurane and transcardially perfused using 250ml of 0.9% saline. The brains were removed immediately and post-fixed for 2 days in 4% paraformaldehyde in 0.1 M PBS. After post fixation, the brainstem was precut by razor blade and sectioned in vibratome with 50µm thickness (VT1200S, Leica, U.S.A). Sections were washed with TBS buffer 3 times for 5 minutes and subjected to antigen retrieval using 1X SignalStain® Citrate Unmasking Solution (Cell signaling). The citrate buffer was bought to boiling temperature and added to the sections. The well plate was incubated at 85°C for 10 min. The plate was allowed to cool down and the sections were washed with TBST buffer (1X TBS buffer + 0.025% tween 20). 5% normal donkey serum and 0.3% Triton-X100 in TBS buffer was used as blocking buffer and the sections were blocked for 1 hour at room temp. Sections were first stained with c-fos and then Choline Acetyltransferase (ChAT) was performed subsequently. C-Fos staining was the done by incubating the sections with the c-Fos antibody (Abcam, ab190289) at 1:1000 dilution in blocking buffer for 3 days placed in shaking incubator at 4°C. Section were rinsed with the TBST buffer 3×5 times and incubated in the donkey anti-rabbit secondary antibody labeled with alexa-fluro 488 (1:500) in blocking buffer for 2 hours at room temperature. Sections were washed 3×5 minutes in TBST buffer and incubated with ChAT antibody (Sigma, AB144) at 1:100 dilutions overnight at 4°C in the blocking buffer. Sections were rinsed the next day with 3×5 minutes in TBS buffer and incubated with anti-goat secondary antibody labelled with alexa fluro 555 (1:200) for 2 hours in room temperature. Sections were rinsed in TBST buffer 3 times and incubated with DAPI 1:1000 dilution in TBS buffer for 1 hour at room temperature. The section was then rinsed two times with TBS buffer and mounted on to Poly-L-lysine coated glass slides. Cover glass was secured on the top of the sections with VECTASHIELD® PLUS Antifade Mounting Medium (Vector labs, H-1900). Sections from naïve, sham and different VNS treatment group were processed in parallel.
c-Fos and ChAT expression in the nucleus tractus solitarius (NTS) and dorsal motor nucleus of the vagus nerve (DMV) was captured using all-in-one fluorescence microscope under 20X objective (BZ-X800, Keyence, U.S.A.). After processed by commercial imaging stitching software (BZ-X800 Analyzer), the orientation of the stitched images was first adjusted for

cross-animal comparison and consistency. To correct non-uniform illumination and attenuate background, the original image was subtracted from background approximation image estimated from morphological opening method. Cells expressing c-Fos and ChAT were counted bilaterally in 3-4 sections/brain using customized cell count tool, with sections taken across -13.68mm ± 250µm according to Breagma, with ROIs for NTS and DMV regions were marked by anatomical expert. Counting was performed bilaterally and represented by counts per regions by an investigator blinded to the treatment conditions. All the post-processing techniques were performed using MATLAB 2016a.

Finite element model of kilohertz electrical stimulation

All simulations were implemented in COMSOL Multiphysics v. 5.4 (COMSOL Inc., Burlington, MA). Our nerve fiber model structure and parameters were adapted from the McIntyre, Richardson and Grill (MRG) model[43] and the Schwarz, Reid and Bostock (SRB) model[44]. Two major nerve fiber subtypes were simulated; myelinated A fiber and unmyelinated C fibers. Ion channels are modelled on the nodes of Ranvier, based on the formulations of the SRB model according to

$$i_{ion} = i_{Na} + i_{Kf} + i_{Ks} + i_L$$

As shown in Figure S7A, the extracellular environment was modelled by a 1000-µm long, 40-µm diameter cylinder surrounding the 1D nerve fiber [45]. Two 50-µm electrodes (50 µm apart) were placed on the surface of the cylinder with the electrode edges forming a 60° angle with the nerve fiber. The first electrode was the cathode and the second electrode was designated as ground.

The stimulus waveform included a wide range of frequency ranging from 0.1-KHz to 12-KHz sinusoid KES, with a duration of 50 ms. A no-flux boundary condition was implemented for V_i and V_e at the ends of the fiber. The mesh setting for myelinated fibers was set to a total of 20 elements for each myelin segment and a size of 0.5 µm for each node segment. The mesh setting for nonmyelinated fibers was a total of 20 elements for each fiber segment, defined as being the same length as the myelin segments of the myelinated fibers. The length of nodes was set to 1 µm in all myelinated fibers[43]. The length of the myelin compartment was also modelled as a function of the myelin diameter [43,46]. The node and myelin diameters used in the model were estimated based on obtained histological data from rat cervical nerves[46]

Node and myelin structures in the model fibers were characterized by different partial differential equations (PDEs). Myelin was approximated by a resistor in parallel with a capacitor (Fig. S7B). We approximated the MRG double cable structure by a single-cable model of the vagus nerve to reduce the computational complexity. The membrane dynamics at the node follows SRB formulations. Models for all fiber types shared ion channel parameters but had fiber-specific physical parameters. All model parameters are listed in Table S3.

The extracellular potential distribution V_e was calculated using:

$$\nabla\left(-\frac{1}{\rho_n}\nabla(V_e)\right) = 0$$

where ρ_n is the nodal resistivity. The intracellular potential V_i was calculated separately for the myelin and node compartments:

$$-\nabla\left(\frac{r_n}{\rho_n}(\nabla V_i)\right) + 2C_n\frac{\partial V_i}{\partial t} = -2\left(i_{ion} - C_n\frac{\partial V_e}{\partial t}\right)$$

$$-\nabla\left(\frac{r_{my}}{\rho_{my}}(\nabla V_i)\right) + 2C_{my}\frac{\partial V_i}{\partial t} = 2C_{my}\frac{\partial V_e}{\partial t}$$

where r_n and r_{my} are the nodal and myelin radius respectively. Membrane potential V_m was determined from the difference between the intracellular and extracellular potentials.

Results

We used 2 stimulus manipulations to target activation of A, B and C vagal fiber types: waveform manipulation and frequency manipulation. For waveform manipulation, we considered 3 different waveforms, at different stimulus intensities: short square pulses (SP, 100 µs pulse width), long square pulses (LP, 600 µs pulse width) and quasi-trapezoidal pulses (QT, consisting of a 100 µs-long plateau and a 2500 µs-long exponentially-decaying falling phase). The performance of the 3 waveforms with respect to fiber selectivity was evaluated by recording eCAP responses to random sequences of single stimuli of the 3 waveforms, to compile neural selectivity indices (NSIs) for each of 3 fiber types (A, B and C), and by collecting fiber-specific physiological responses to trains of stimuli, to compile corresponding physiological selectivity indices (PSIs). With waveform manipulation, we were able to selectively engage A-fibers (SP stimuli), or B-fibers with minimal or no engagement of A- or C-fibers (LP and QT stimuli). For frequency manipulation, we delivered trains of square pulse stimuli at different frequencies in the KHz range, at several intensities and compared them to intensity-matched stimulus trains with 30 Hz pulsing frequency, further identify the cut off value of frequency that elicit distinct physiological response patterns other than low frequency range. The performance of KHz pulsing frequency with respect to fiber selectivity was evaluated by compiling PSIs, using physiological responses to stimulus trains, by compiling NSIs using eCAP responses to test pulses probing fiber excitability, and by histologically assessing activation of neural populations in the brainstem associated with different fiber types. Using frequency manipulation, we were able to selectively engage C-fibers at frequencies above 5-KHz, with reduced engagement of A- or B-fibers, and the results were further validated by c-Fos expression in brainstem associated with VN. Both waveform and frequency manipulations were tested in 2 rodent species, rats and mice, with similar results. Finally, a possible role for sodium ion channels in the C-fiber selectivity of KHz-range frequency stimuli was explored in a computational model of unmyelinated vagal fibers.

Waveform manipulation allows selective activation of A- and B-fibers

It has been demonstrated before[22,23] that single-pulse stimuli elicit eCAPs that depend on stimulus waveform, intensity and polarity configuration (Fig. 1). In cathode-corner polarity, the fiber recruitment order is usually A-, followed by B-fibers, with no evidence of C-fiber engagement; fiber amplitude is monotonically increasing with stimulus intensity for all 3 waveforms, SP, LP and QT (Fig. 1A, panels a-c). In the cathode-center polarity, SP stimuli produce the same fiber recruitment order, though the response is greater than with cathode-corner stimuli of the same stimulus intensity (Fig. 1A-d). With the same polarity, LP and QT stimuli of increasing intensity produce progressively smaller A-fiber responses, whereas B- and C-fiber responses, once elicited, become progressively larger (Fig. 1A-e and 1A-f, respectively). Intensity at intermediate levels for both LP and QT stimuli are associated with greater activation of B-fibers compared to that of A- or C-fibers (Fig. 1A panels, panels e-f). The statistics of normalized amplitude associated with fiber responses demonstrate the same trend (Fig. 1B). To quantify the degree of A-, B- and C-fiber selectivity of each of the 3 waveforms, we compiled fiber type-specific neural selectivity indices (NSIs), with the targeted fiber in the numerator and the non-targeted fibers in the denominator. For A-fibers, maximum NSI is achieved at threshold intensity with all 3 waveforms, but is highest with SP stimuli (Fig. 1C). For B-fibers, SP has the worst performance, with a moderate increase at higher intensities, LP and QT waveforms have maximal NSIs at intermediate intensity levels and QT outperforms the other 2 in terms of maximum NSI and average NSI across all intensities (Fig. 1D). Intensities of 3-6×NT for LP and 4-7×NT for QT stimuli are associated with greater activation of B-fibers compared to that of A- or C-fibers.

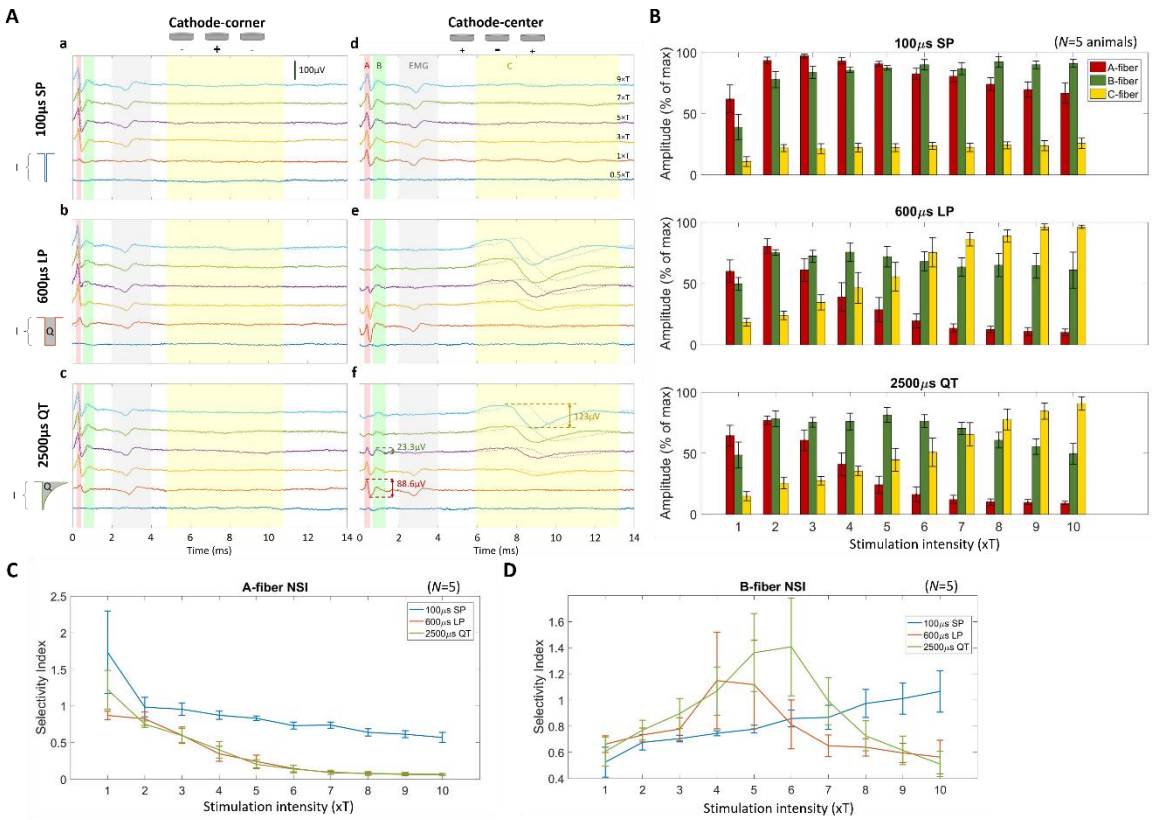

Figure 1: Vagal stimulus-evoked compound action potentials (eCAPs), fiber activation amplitudes and resulting neural selectivity indices (NSIs) in response to A- and B-fiber-selective stimulus waveforms, in the rat model.

(A) Representative eCAPs evoked by different stimulus waveforms: 100 µs square pulse (short square pulse, SP; panel a, d), 600 µs square pulse (long square pulse, LP; panel b, e), and 100 µs-plateau followed by a 2500 µs exponentially decaying pulse (quasi-trapezoidal pulse, QT: panel c, f). Shown are representative eCAP examples in response to cathode-center and cathode-corner polarities and a range of stimulus intensities, from 1 to 10 times thresholds (×NT) in a single animal. Traces from both proximal (solid) and distal (dash) contacts of the recording electrode are shown and each trace represents the average of triggers. A-, B-, and C-fiber activation and stimulus-evoked EMG activity, are calculated as peak-to trough amplitude of eCAP components with different latencies and their overlap with latency windows corresponding to the conduction velocities of different fibers (A-fiber: red; B-fiber: green; C-fiber: yellow; EMG: grey).

(B) Mean (±SE, N = 5 animals) normalized fiber activity evoked by the 3 stimulus waveforms of cathode-center polarity, at different stimulus intensities, in 5 animals. (Two-way ANOVA, $p<0.05$ for waveform and intensity, across all fibers (A-, B-, C-)),

(C) Mean (±SE, N = 5 animals) NSI values for A-fibers, for each of the 3 stimulus waveforms, as a function of stimulus intensity. (Two-way ANOVA, $p<0.05$ for waveform and intensity)

(D) Same as (C) but for B fibers. (Two-way ANOVA, $p=0.22$ for waveform, $p<0.05$ for intensity)

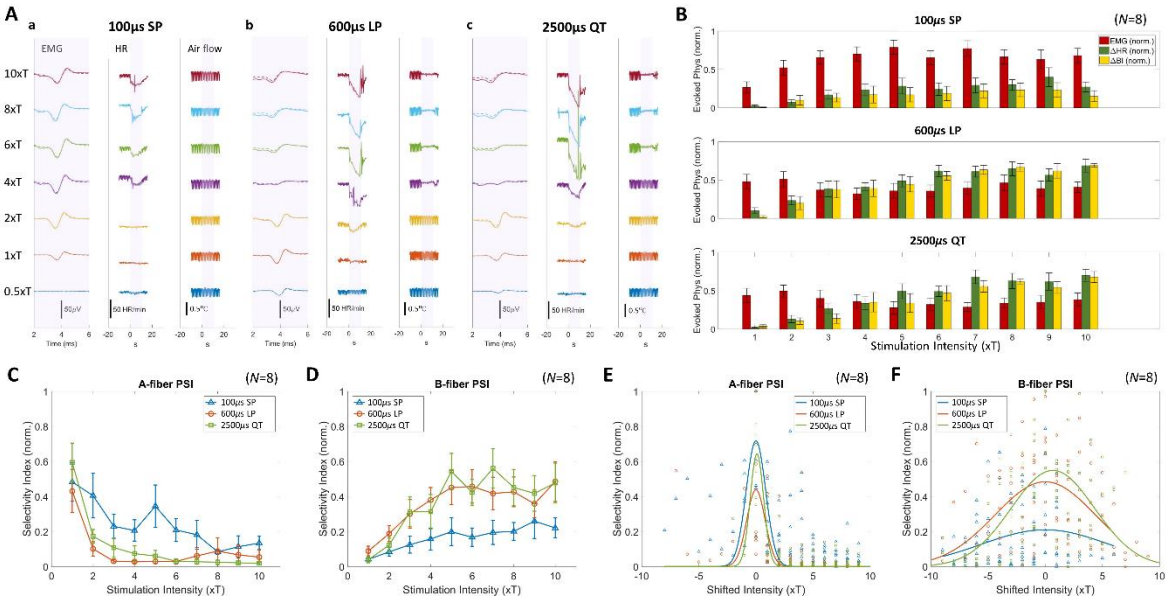

Figure 2: Vagal stimulation-elicited changes in physiological parameters, magnitude of physiological effects and resulting physiological selective indices (PSIs) in response to A- and B-fiber selective stimulus waveforms, in the rat model.

(A) Representative laryngeal EMG (left for each panel), heart rate (HR, middle of each panel), and breathing responses (air flow, right of each panel) elicited by stimulus trains of 3 different waveforms, short pulse (SP), long pulse (LP) and quasi-trapezoidal (QT), for a range of stimulus intensities (0.5 to 10×NT).

(B) Mean (±SE, N=8 animals) normalized EMG (red bars), HR (ΔHR, green bars) and breathing interval responses (ΔBI, yellow bars) elicited by the 3 stimulus waveforms, for different stimulus intensities. (Two-way ANOVA, $p<0.05$ for waveform, across all physiological responses (EMG, HR, BI), $p<0.05$ for intensity, across all physiological responses except for EMG)

(C) Mean (±SE, N=8 animals) normalized A-fiber PSI values associated with each of the stimulus waveforms (SP: blue, LP: red, QT: green trace), as a function of stimulus intensity. (Two-way ANOVA, $p<0.05$ for waveform and intensity)

(D) Same as (C) but for B-fibers. (Two-way ANOVA, $p<0.05$ for waveform and intensity)

(E) Normalized A-fiber PSI values for each of the 3 waveforms plotted against stimulus intensity, re-aligned to the value associated with the maximum PSO for each animal and waveform, so the intensity shift of 0 corresponds the intensity producing the maximum PSI for each animal. Also shown are 1-D Gaussian function fits to the data for each of the 3 waveforms. Rmse for each fits: 0.235(SP), 0.126(LP), 0.111(QT).

(F) Same as (E) but for B-fiber PSI values. Rmse for each fits: 0.188(SP), 0.240(LP), 0.254(QT).

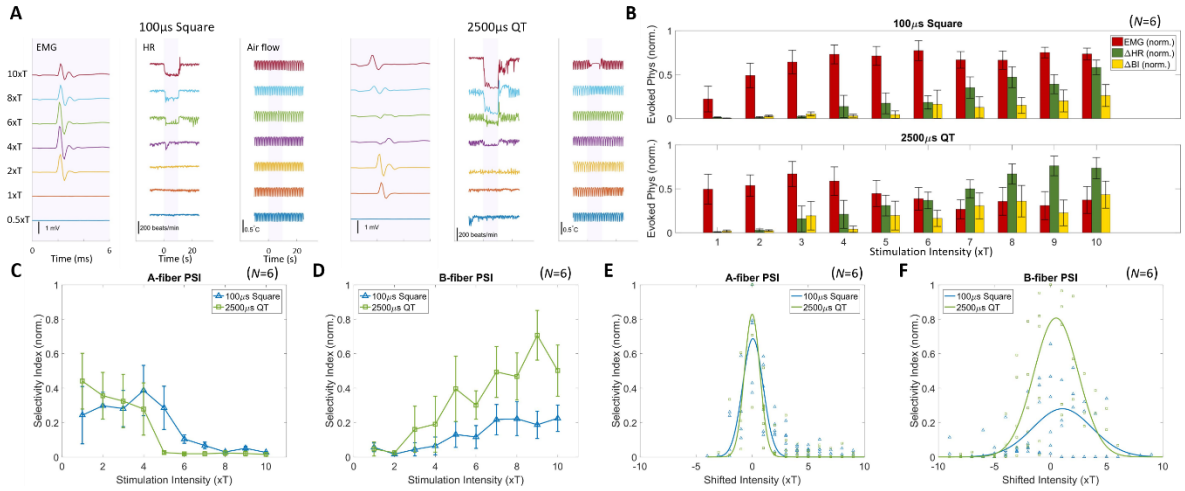

Figure 3: Vagal stimulation-elicited changes in physiological parameters, magnitude of physiological effects and resulting physiological selective indices (PSIs) in response to A- and B-fiber selective stimulus waveforms, in the mouse model.

(A) Representative laryngeal EMG (left for each panel), heart rate (HR, middle of each panel), and breathing responses (air flow, right of each panel) elicited by stimulus trains of 2 different waveforms, short pulse (SP) and quasi-trapezoidal (QT), for a range of stimulus intensities (0.5 to 10×PT(EMG), close to NT).

(B) Mean (±SE, N=6 animals) normalized EMG (red bars), HR (ΔHR, green bars) and breathing interval responses (ΔBI, yellow bars) elicited by the 2 stimulus waveforms, for different stimulus intensities. (Two-way ANOVA, $p<0.05$ for waveform, across all physiological responses (EMG, HR, BI), $p<0.05$ for intensity, across all physiological responses except for EMG)

(C) Mean (±SE, N=6 animals) normalized A-fiber PSI values associated with each of the stimulus waveforms (SP: blue, LP: red, QT: green trace), as a function of stimulus intensity. (Two-way ANOVA, $p<0.05$ for waveform and intensity)

(D) Same as (C) but for B-fibers. (Two-way ANOVA, $p<0.05$ for waveform and intensity)

(E) Normalized A-fiber PSI values for each of the 2 waveforms plotted against stimulus intensity, re-aligned to the value associated with the maximum PSO for each animal and waveform, so the intensity shift of 0 corresponds the intensity producing the maximum PSI for each animal. Also shown are 1-D Gaussian function fits to the data for each of the 3 waveforms. Rmse for each fits: 0.134(SP), 0.128(QT).

(F) Same as (E) but for B-fiber PSI values. Rmse for each fits: 0.140(SP), 0.224(QT).

When delivered as stimulus trains (10 s duration, 30 Hz) the 3 waveforms produce, distinct types of physiological responses resulting from activation of different fibers: EMG results from A-fiber activation, changes in heart rate (ΔHR) from B-fibers and changes in breathing interval (ΔBI) from C-fibers (Fig. S2)[40]. With SP stimuli, increasing intensity results in increasing, and eventually saturating EMG, with modest ΔHR and ΔBI responses at higher intensities (Fig. 2A-a, Fig. 3A/mouse). With LP and QT stimuli, EMG is suppressed, all the while robust ΔHR and ΔBI responses are elicited (Fig. 2A, panels b and c, Fig. 3A/mouse). Overall, trains with SP stimuli produce the largest EMG responses across all stimulus intensities, while trains with

LP and QT stimuli produce larger ΔHR and ΔBI responses, especially at intermediate and higher intensities, with significantly smaller EMG effects (Fig. 2B, Fig. 3B/mouse). When the 3 types of physiological responses are combined into fiber-specific physiological selectivity indices (PSIs), SP stimuli are on average more selective for A-fibers (Fig. 2C, Fig. 3C/mouse), and LP and QT stimuli are more selective for B-fibers (Fig. 2D, Fig. 3D/mouse). The intensity levels associated with peak PSI values for A-fibers are typically in the range 1-3×PT, and for B-fiber in a wider range, varying across animals. When PSI curves from each animal are aligned at the "optimal" intensity, PSI falls symmetrically with intensity around the peak value (Fig.2E/3E and 2F/3F, for A- and B-fibers in rat/mouse respectively). At optimal intensity, QT outperforms the other 2 waveforms in terms of its B-fiber selectivity (One-way ANOVA, $p<0.05$, Fig. S3, Fig. S4/mouse), consistent with NSI findings in rat.

Frequency manipulation allows selective activation of C-fibers

KHz-range electrical stimulation (KES), has been used to block conduction in vagal fibers according to their diameter, including small C-fibers[35]. We sought to assess whether KES can be used to activate vagal C-fibers, while minimally activating larger, A- and B-fibers. Physiological responses to KES trains of different frequencies were compared to those elicited by 30 Hz trains of the same duration, intensity and PW (Fig. 4). ΔHR and ΔBI effects of 1-KHz trains are similar in magnitude to those of 30 Hz trains (Fig. 4A-c), indicating similar levels of activation of B- and C-fibers, respectively. At 5-Khz and 12.5-KHz, high intensity stimulation results in similar ΔBI responses as 30-Hz trains ($p>0.05$) but with minimal ΔHR responses ($p<0.05$), indicating engagement of C-fibers without engaging B-fibers (Fig. 4A-a, b). On average, across a wide range of intensities, the higher the frequency, the smaller the ΔHR effect similar ΔBI effects (Fig. 4B). To determine the frequency and intensity cut-off values beyond which selective C-fiber activation occurs, trains of stimuli with identical pulse width (40μs) were delivered at different KHz-range frequencies and intensities. At frequencies of 5-KHz or above, ΔHR responses across intensities were minimal (Fig. 4C), whereas significant ΔBI responses were registered at high intensities, 8-10×PT (Fig. 4D). In experiments in mice, KES of increasing intensity elicited similar ΔBI effects as 30 Hz stimulation, with large intensity (15-25×PT), but with a much smaller ΔHR response and stronger suppression at low intensity (1-3×PT) (Fig. 6A).

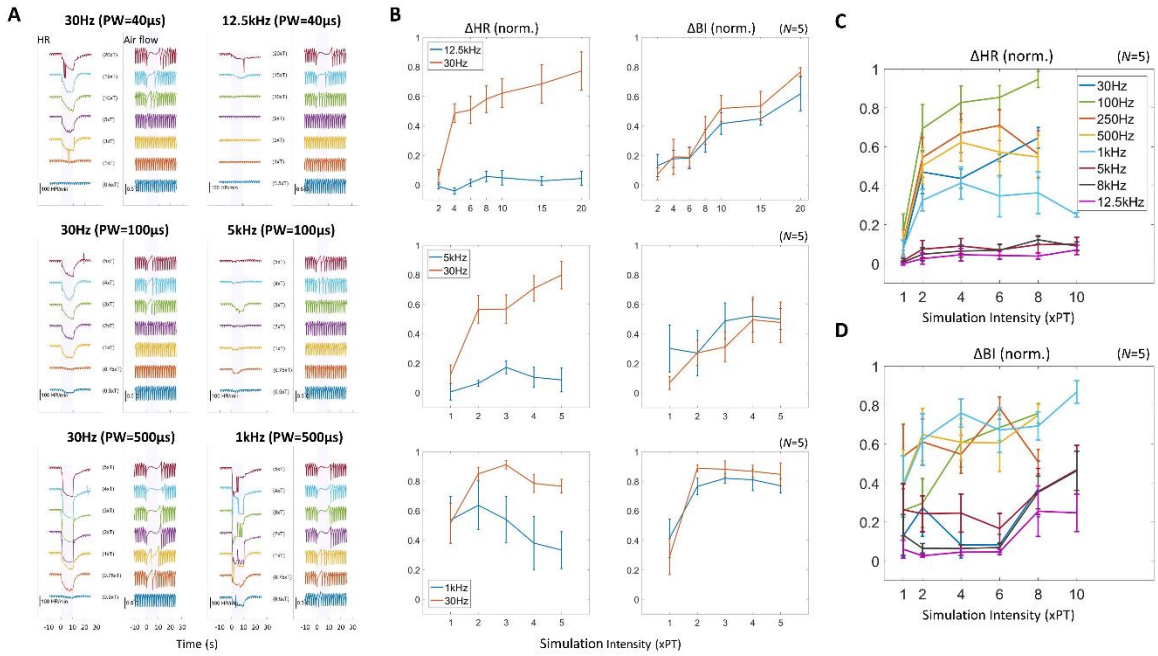

Figure 4: Physiological responses to vagal stimulus trains of different KHz-frequencies, compared to 30Hz trains of stimuli with comparable pulse widths (PW), in the rat model.

(A) Representative heart rate (HR) and breathing responses (airflow) elicited by stimuli of 3 different KHz-frequencies: 1KHz (500 µs PW), 5KHz (100 µs PW) and 12.5KHz (40 µs PW), next to their 30 HZ, PW- and intensity-matched controls from the same animal (panels a, b and c, respectively). All stimulus trains were 10-s-long, as marked by the light blue-shaded areas.

(B) Mean (±SE, N = 5 animals) normalized ΔHR and ΔBI responses for each of the 3 frequency stimuli (1 KHz, 5 KHz, 12KHz; blue curves in panels a, b and c, respectively) along with responses to their corresponding 30 Hz controls (red curves in each panel), as a function of stimulus intensity. (HR: Two-way ANOVA, $p<0.05$ for all frequency pairs, $p<0.05$ for intensity except for 1KHz vs 30Hz pairs. BR: Two-way ANOVA, $p>0.05$ for all frequency pairs, $p<0.05$ for intensity)

(C) Mean (±SE, N = 5 animals) normalized ΔHR responses to trains of stimuli of varying frequencies (ranging from 30Hz to 12.5Hz, shown in different color curves) and of identical PW (40 µs), as a function of stimulus intensity. (Two-way ANOVA, $p<0.05$ for frequency and intensity)

(D) Same as (C) but for normalized ΔBI responses. (Two-way ANOVA, $p<0.05$ for frequency and intensity)

To document fiber excitability changes that could explain the fiber-specific physiological responses to KES, single "probing" pulses were delivered at regular intervals (1-s) throughout KES trains, at 8-KHz, and resulting eCAPs were compiled. Short-width probing pulses (100 µs) elicit A- and B-fiber responses that abruptly disappear at KES intensities above 3×PT and 7×PT, respectively (Fig. 5A). Long-width probing pulses (600 µs) elicit C-fiber responses, which are progressively suppressed as KES intensity increases (Fig. 5B). Overall, both A-fibers and EMG responses are suppressed at intensities between 1-3×PT (red bars in Fig. 5C, D). B-fibers are progressively suppressed between 1-8×PT, which correlates with the minor moderate

ΔHR responses seen at those intensities (green bars in Fig. 5C, D); notably, ΔHR responses are sustained but minor at intensities >8×PT (Fig. 5D). C-fibers are also suppressed progressively as intensity increases, but at a slower rate than A- or B-fibers; at the same time, ΔBI responses gradually increase (yellow bars in Fig. 5C-a, b). This slower suppression rate, along with the gradual engagement of more C-fibers by stimuli of increasing intensity, creates an "intensity window" (7-20×PT) in which A- and B-fibers are maximally suppressed, and C-fibers are partially suppressed but still excitable. Similar findings are found in mice, though optimal intensities for C-fiber activation are generally higher (10-30×PT, Fig. 6B); of note, threshold intensities in mice were much smaller than in the rat (11.6μA vs 221.4 μA). This is further demonstrated by NSIs and PSIs for each fiber type: for A- and B-fibers, they both decrease with increasing KES intensity (Fig. 5E-a, b, respectively), whereas for C-fibers, both indices are maximal at KES intensities >7×PT (Fig. 5D-c, Fig. 5E). In mice, we found more varying intensities associated with ΔHR response suppression and ΔBI responses across animals, thus leading to more distinct optimal window for C-fiber, but the trend remained similar (Fig. 6C, D). It is worth noting here that we calculated PSIs with EMG set to constant (0.5) here, as we were not able to obtain laryngeal EMG under continuous KES condition. To test whether addition of probing pulses to KES trains altered the patterns of physiological responses, in some rats, we compared the physiological responses, ΔHR and ΔBI, to KES alone (without probing pulses) with the responses to KES with 100 or 600 μs-long probing pulses. No significant differences were found, across a range of KES intensities (Fig. S6).

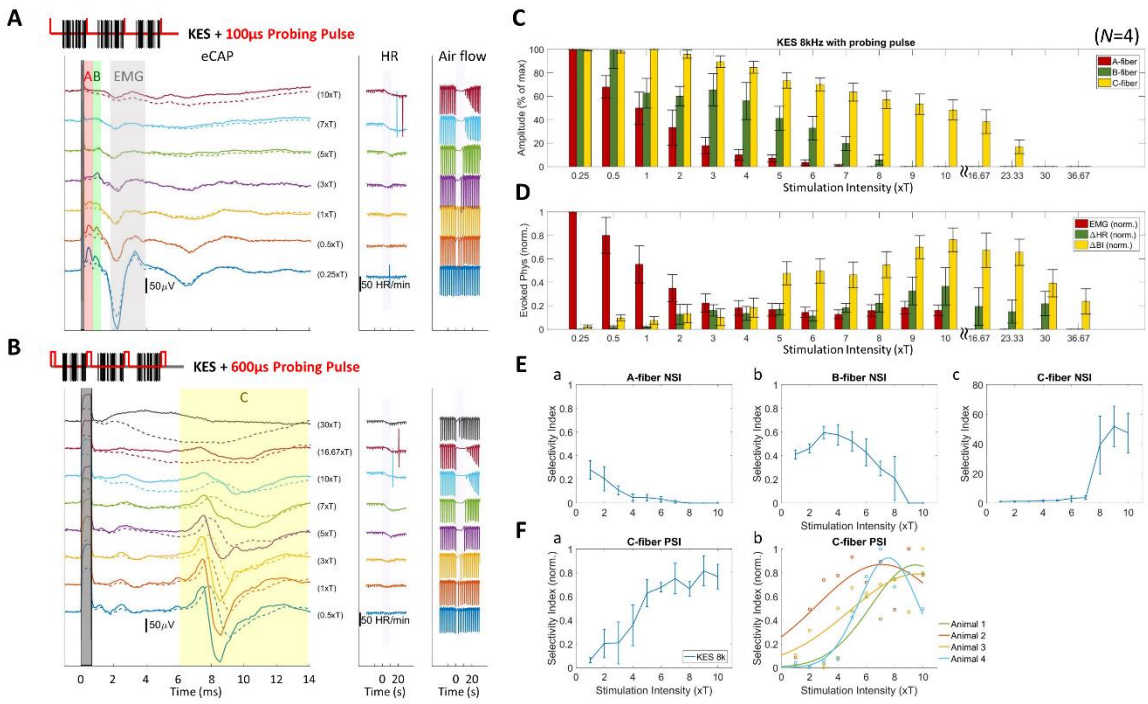

Figure 5: eCAPs, elicited physiological effects and resulting neural and physiological selectivity indices (NSI and PSI), in response to 8-KHz frequency electrical stimulation of the vagus (KES) of different intensities, in the rat model.

(A) Representative eCAPs, ΔHR, and ΔBI responses by KES in a single animal, at different stimulus intensities (0.25 to 10×PT). eCAPs were compiled by delivering, concurrently with KES, single, monophasic, 100 μs-long "test" pulses every 1 s, 10 times in total, to evoke A-fiber and laryngeal EMG activity. Stimulus intensities are expressed in units of threshold intensity, defined as the PT of KES (0.5 to 10×PT).

(B) Same as (A), but with 600 µs-long test pulses delivered concurrently with KES, to evoke C-fiber activity.

(C) Mean (±SE, N = 4 animals) of normalized amplitude of A-, B-, C-fiber activity (red, green and yellow vars, respectively) evoked by test pulses (100 µs: A- and B-fiber, 600 µs: C-fiber), during KES of different intensities. (One-way ANOVA, $p<0.05$ for intensity, across all physiological responses (EMG, HR, BI))

(D) Mean (±SE, N = 4 animals) of normalized magnitude of physiological responses (EMG, red; ΔHR, green; ΔBI, yellow), elicited by KES of different intensities, in 4 animals. (One-way ANOVA, $p<0.05$ for intensity, across all fibers (A-, B-, C-))

(E) Mean (+/-SE) values of NSI for A- (a), B- (b) and C-fibers (c) as function of KES intensity, in 4 animals. (One-way ANOVA, $p<0.05$ for intensity, across all types of NSI)

(F) Normalized PSIs for C-fibers as function of KES intensity (a) Mean (+/-SE) values of normalized PSIs. (One-way ANOVA, p<0.05 for intensity) (b) Normalized PSI values for C-fibers cross animals, and Gaussian function is fitted to show the distribution of PSIs evoked by KES stimulus. Average Rmse for the fits: 0.169.

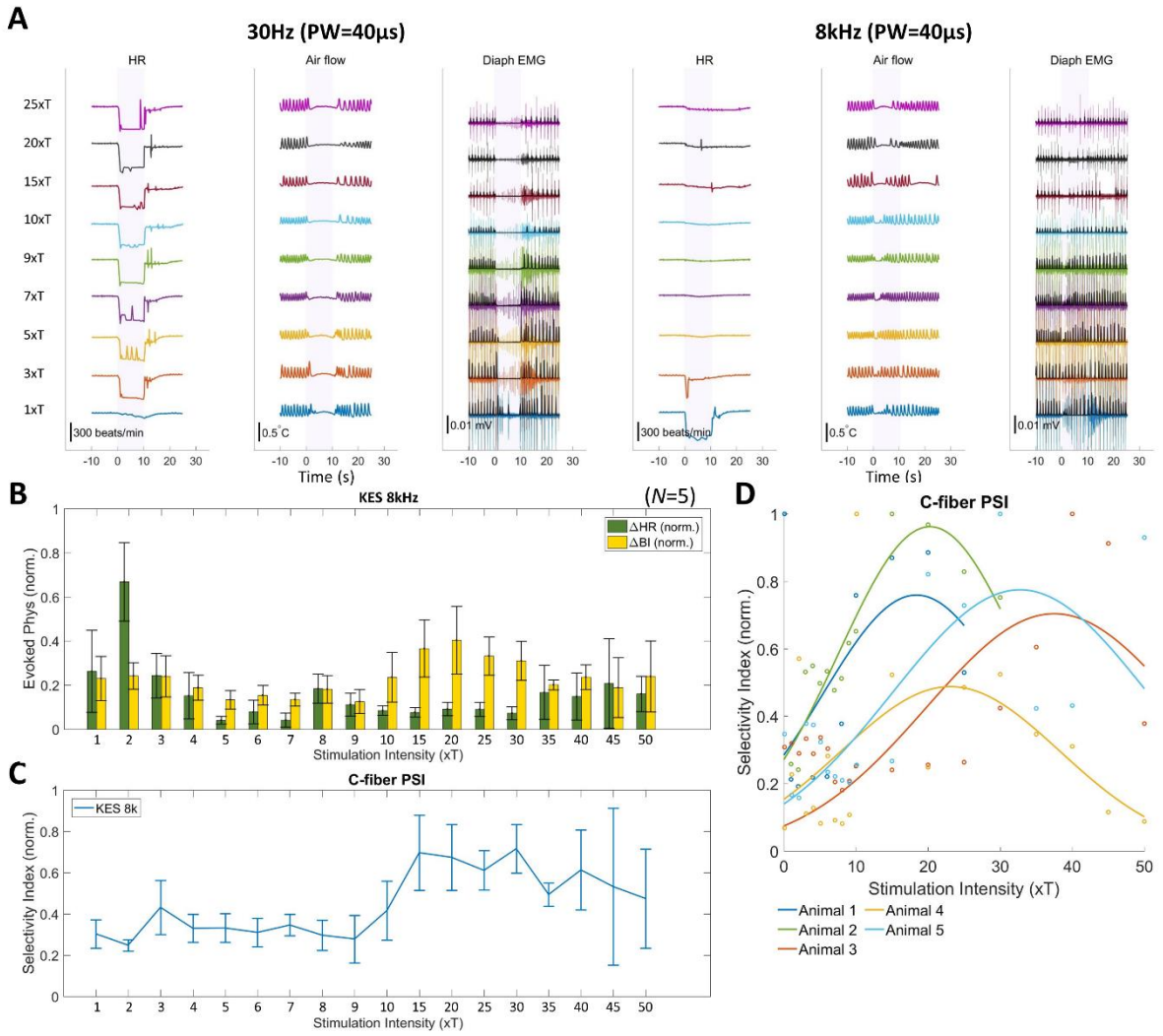

Figure 6: Elicited physiological effects and resulting physiological selectivity indices (PSI), in response to 8-KHz frequency electrical stimulation of the vagus (KES) of different intensities, in the mouse model.

(A) Representative ΔHR, ΔBI, and diaphragm EMG (associated with breathing pattern) responses by 30Hz and KES in a single animal, at different stimulus intensities. Stimulus intensities are expressed in units of threshold intensity, defined as the PT of KES (1 to 25×PT).

(B) Mean (±SE, N = 5 animals) of normalized magnitude of physiological responses (ΔHR, green; ΔBI, yellow), elicited by KES of different intensities. (One-way ANOVA, HR: $p<0.05$, BR: $p=0.74$, for intensity)

(C) Mean (+/-SE) values of PSI for C-fibers as function of KES intensity, in 5 animals. (One-way ANOVA, $p<0.05$ for intensity)

(D) Normalized PSI values for C-fibers cross animals, and Gaussian function is fitted to show the distribution of PSIs evoked by KES stimulus. Average Rmse for the fits: 0.211.

Effect of different VNS protocols on brain stem nuclei activity

Even though waveform and frequency manipulations allow preferential activation of different fiber types in the vagus, it is unclear whether such manipulations can also affect the activity level of sensory and motor vagal neurons associated with those fibers. To determine that, we delivered VNS intermittently for 30 minutes (10 seconds on, 50 seconds off), with standard 30 Hz VNS (100µs pulse width, 2mA), or with 8-KHz VNS (40µs, 2mA, 8-10×PT), and measured c-Fos$^+$ immunoreactivity of single neurons in the ipsilateral and contralateral (to VNS) brainstem. In particular, we looked in the nucleus tractus solitarius (NTS), a sensory region, and in the dorsal motor nucleus of the vagus (DMV), a motor region with ChAT$^+$ cells providing efferent cholinergic fibers to the vagus (Fig. 7A). In the ipsilateral NTS, the 30 Hz VNS group has 516.3±32.16 c-Fos$^+$ cells (314% greater than the sham group), whereas the KES group has 358.9±24.83 c-Fos$^+$ cells (188% greater than the sham). In the ipsilateral DMV, 30 Hz VNS resulted in 19.08±1.98 c-Fos$^+$/ ChAT$^+$ cells (900% greater than sham), whereas KES in 8.17±1.52 cells (328% greater than naïve) (Fig. 7C). Interestingly, 30Hz VNS also resulted in a small increase of c-Fos$^+$ cells in contralateral NTS and DMV compared to the sham group (297±44.19 and 4.917±0.95, 131% and 170% compared with sham), whereas KES did not have a significant contralateral effect (Fig. 7B (left), and Fig. 7C(left)). Cell counts in the sham stimulation group were not different than naïve, in neither of the 2 brain regions, ipsilateral or contralateral (Fig. 7B and 7C). Overall, 30 Hz VNS resulted in increased cell activation in ipsilateral NTS and even more in ipsilateral DMV, indicating a more "efferent selective" effect, whereas KES resulted in a comparable increase cell activation in NTS with a much smaller activation in DMV, indicating a more "afferent-selective" effect (Fig. 7D).

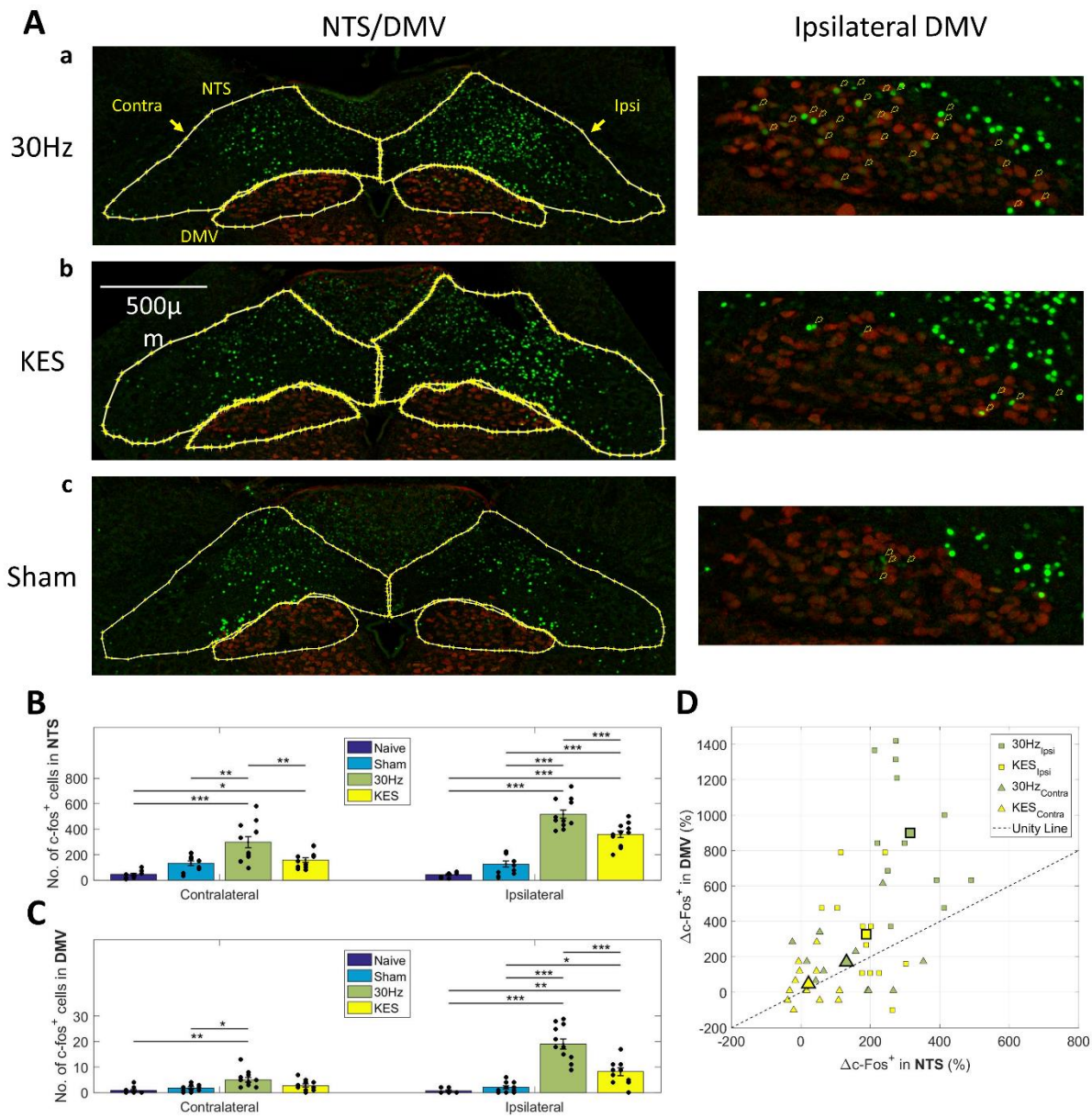

Figure 7: c-Fos expression in sensory and motor vagal brainstem regions after 30Hz and 8 KHz VNS, in the rat model.

(A) Representative immunohistochemistry images of sections across ipsilateral and contralateral, to VNS, sensory and motor brainstem regions (yellow contours): nucleus tractus solitaries (NTS) and dorsal motor nucleus of the vagus (DMV) (anterior-posterior: -13.68mm ±250µm relative to Breagma, medial-lateral: ±2mm relative to mid sagittal plane, dorsal-ventral: 7.2-8.2mm relative to brain vertex), each stained for c-Fos (green) and ChAT (red). Inset show ipsilateral DMV at higher magnification; arrows point to cells positive for c-Fos. (a) After 30 min of intermittent 30 Hz VNS (10-s ON and 50-ss OFF, 30 cycles). (b) After 30 min of intermittent 8 KHZ VNS (KES), of the same cyclic settings. (c) After sham stimulation (electrode placed on nerve, no stimulation delivers)

(B) c-Fos$^+$ cell numbers (mean±SE) in contralateral and ipsilateral NTS, in different group of animals: naïve (dark blue), sham stimulation (light blue), 30 Hz VNS (light green), KES (yellow). Each group consisted of 3 animals and each animal contributed 3-4 sections from

which cell numbers were calculated. Statistical comparisons between groups used one-way ANOVA and Tuckey's post-hoc tests (*p<0.05, **p<0.005, ***p<0.0005).

(C) Same as (B), but for DMV.

(D) Normalized c-Fos$^+$ cell numbers (% difference in c-Fos$^+$ cell numbers with respect to average cell numbers in sham group) counted in DMV vs. those counted in NTS (ipsilateral: square dots, contralateral: triangle dots), from all sections from 30 Hz VNS group of animals (green dots) and from the KES group of animals (yellow dots). Mean values shown with black outlined dots.

Simulating the potential mechanisms underlying differential fiber activity under KES.

Given the reported contribution of voltage-gated sodium channels in KES-induced neural activities in the central and peripheral nervous systems[47-50], we sought to determine whether sodium channels could be at least in part responsible for the obtained selectivity in this study. In particular, we speculate that different physical properties in myelinated and unmyelinated fibers might result in the characteristic sodium channel activation or blocking under KES. We simulated voltage responses to KES of a large, myelinated fiber, representative of efferent A-fibers (myelin diameter: 5-µm, axonal diameter: 2.6-µm) and of a small, unmyelinated fiber, representative of afferent C-fiber (axonal diameter: 1.3-µm), both placed at the same radial distance from the stimulating electrode (Fig. S7). The physical parameters of the two fibers were estimated based on our obtained histological data from rat cervical nerves (see Fig. S8). Our simulations showed that the two fiber types respond remarkable differently to KES, across a range of frequencies and intensities (Fig. 8A). Below 1-KHz, no fiber blockage is observed. Both fiber types are monotonically recruited with increase of intensities, and end with spike saturation (Fig. 8A, panels from 0.1-KHz to 1-KHz). Starting at 2-KHz, the large myelinated fiber is initially activated (at intensities between 2.5 and 5µA) followed by a falling phase (between 4 and 6µA). However, the small unmyelinated fiber was activated later at intensities higher than 6µA. The "excitation windows" of the two fibers demonstrated a minimized overlap (Fig. 8A, panel 2-KHz). The separation between the two excitation windows is further increased at higher KHz-frequency stimuli, e.g. 4-KHz and 8-KHz (Fig. 8A, panels 4-KHz and 8-KHz), ultimately stabilizing at 12-KHz (Fig. 8A, panels 12-KHz). At high Khz frequencies (e.g. 8-KHz), large fibers are strongly activated at low intensities (Fig. 8A, Fig. 8B-a1), and blocked at intermediate intensities where membrane voltage start passively following the stimulus current without any elicited action potentials (APs) (Fig. 8B-a2, a3). Under the same stimulation condition, small unmyelinated fibers remain inactivated at low and intermediate intensities (Fig. 8B-a4, a5) and are increasingly recruited at higher intensities, with robust generation of APs (Fig. 8B-a6). The KES-induced differential excitability between myelinated and unmyelinated fibers predicted by our modeling closely agrees with *in vivo* electrophysiology.

In addition, the simulated selectivity was also indicated by their differential sodium channel dynamics under identical KES parameters. When myelinated fibers are blocked (Fig. 8B-a2, a3), the sodium channel activation (m^3) and inactivation (h) gating variables become entrained with the extracellular voltage that is changing according to the KES (Fig. 8B-b2, b3). Under the same stimulation condition, m^3 and h in unmyelinated fibers remained at steady states (Fig. 8B-b4, b5), and indicate physiological opening and closing at increasing intensity (Fig. 8B-b6).

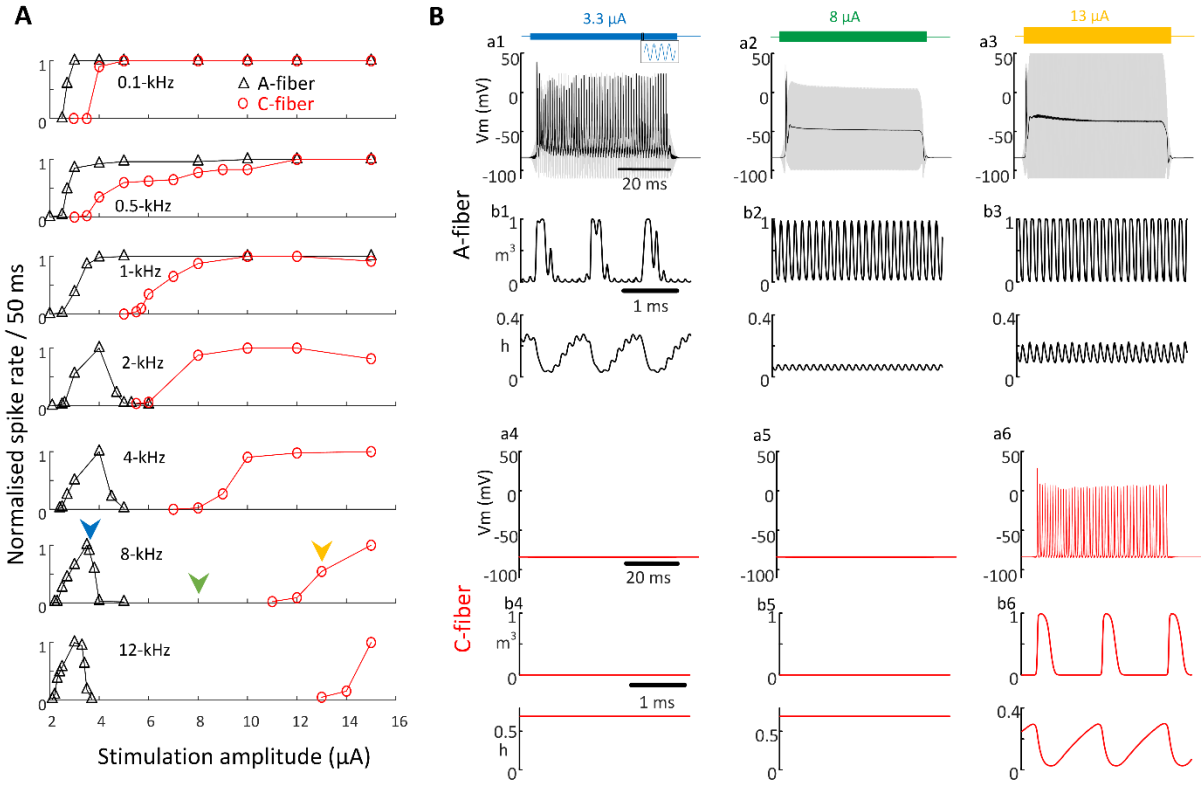

Figure 8: Computational simulation of KES for different type of fibers.

(A) Normalized spike rate elicited at myelinated (A-fiber) and un-myelinated (C-fiber) fiber models using 0.1-KHz, 0.5-KHz, 1-KHz, 2-KHz, 4-KHz, 8-KHz and 12-KHz sinusoid KES, across multiple intensities.

(B) Examples of induced blocking and excitation AP activities (a) and steady-state activation (m^3) and inactivation (h) gating variables (b) of sodium current (neurites below the electrode) during 8-KHz KES for two types of fibers (A-fiber: 1-3, C-fiber: 4-6). The activities were simulated at the stimulation amplitudes indicated by the arrows in panel (A), from low (blue), intermediate (green), to high intensity (yellow). The raw membrane activities with stimulation artifacts were shown using grey shadow.

Discussion

We have leveraged both waveform and frequency modulation stimulation strategies to achieve selective VN activation for different fiber types, and validated the results through evoked compound action potentials (eCAPs) and corresponding physiological effects, including laryngeal electromyography (EMG), heart rate (HR) changes and breathing rate (BR) changes. We further optimize the selectivity of each type fiber by computing its NSIs and PSIs, aiming to maximize desire and minimized off-target effect simultaneously. Results indicate that the A-fiber selectivity can be simply achieved by applying low frequency (30Hz), low intensity of stimulation and almost independent of stimulation parameters as long as the delivered charge is enough (Fig.1C, 2C and 2E/rat, 3C and 3E/mouse). To target B-fiber, longer square pulse or QT pulse is required (Fig. 1D, 2D and 2F/rat, 3D and 3F/mouse); however only a relatively narrow optimal intensity window is effective and varied from animals to animals. The C-fiber response is more sensitive to frequency manipulation and can be targeted specifically through high dose of KES (>5-KHz) (Fig. 5E and 5F/rat, 6C and 6D/mouse).

Anodal block and waveform manipulation for A- and B-fiber selective activation

For extracellular electrical stimulation, such as non-invasive cuff electrode for most of clinical VNS applications, the fiber recruitment generally follows a size principle: myelinated fibers with largest diameter (A-fiber) are recruited first and those unmyelinated with the smallest diameter (C-fiber) are recruited last; therefore, there is never an issue to achieve A-fiber selectivity as it is a build-in nature of peripheral nerve fiber. Most of the FDA-approved therapy for VNS, such as epilepsy and depression, are most likely associated with the A-type afferent fiber[51]. B-fiber selectivity is relatively challenging as A-fibers generally have lower thresholds for wide parameter range, and most likely the main reason that fails the VNS in B-fiber related applications, such as heart failure, as several serious side effect like hoarseness, coughing, and neck pain are mediated by activation of A-fibers[21,52]. Anodal block and waveform manipulation have been used to selectively target slower myelinated fibers through limiting the propagation of the fastest fiber. Previous study in vagus nerve stimulation have shown that the QT (or exponential falling) pulse, with tripolar stimulation configuration, can effectively suppress the evoked EMG activity and associated with the A-fiber recruitment[22,26]. Moreover, a more recent study focusing on afferent versus efferent physiological effects to VNS, has demonstrated that the direction of activation of A- and B-fiber can be biased through anodal block with proper inter-electrode distance and pulse width setting[23]. Our results are consistent with previous findings, as both long duration and QT pulse with adequate intensity range can effectively attenuate both A-fiber response and evoked EMG. We further found that with the same intensity range, which varies across animal, decent amount of B-fiber as well the HR response can be evoked while only minimum C-fiber activity and breathing effect were observed, therefore achieving more selective activation of B-fibers. The main reason for QT outperforming the long square pulse in terms of B-fiber is that QT can induce relatively less C-fiber activation under same charge injection while similar amount of B-fiber and HR changes can still be reached. However, one drawback for waveform manipulation is that the optimal intensity range for preferential excitation and inhibition varies across animals, potentially related to the proximity between target fiber and active/return electrode, and critically dependent on the robustness of neural interface. As the result. these solutions may be less suitable when applying to chronic condition, especially the beginning of post-implant period which generally shows significant threshold change due to foreign body reaction[53], or scaling to more complex large diameter nerves in the human or large animal model under clinical setting.

KES for C-fiber selective activation

KES is believed to induce reversible inhibition of action potential propagation in peripheral nerve and has been validated in a variety of animal model and nerve diameters[32]. However, the excitation effect resulted from KES was often underestimated, as no proper tool can be used to assess the unsynchronized action potential to the continuous stimuli, except for the patch clamp which is not feasible in single nerve fiber. Generally, to assess the effect of KES, two methods are most commonly used, including measurement of physiological states, such as muscle force[54], EMG activity[55], cardio respiratory parameters[56], or cytokine level[57], and evoked electroneurogram recording with additional electrode to deliver probing pulses[35,57,58]. The measurement of physiological states, although necessary, is not sufficient for ensuring that a true nerve conduction block is achieved by KES nor is the cause of the desired physiological effect, as this could be achieved through a number of other mechanisms[59]. For example, recent reports suggest that the Enteromedics vBloc system, which claims to electrically block subdiaphragmatic vagus nerve activity using KES for treatment of obesity, is likely to achieve the physiological effect (i.e. reduction in weight loss) by continuously activating the nerve, as opposed to blocking it[34]. Similarly, the electroneurogram recording alone, as it only calibrates the nerve response to the probing pulse, might miss the nerve true asynchronous response during the KES period. For example, in retinal study, the retinal ganglion cell spike rates can be directly mediated by KES without extra probing pulse[47].

In our study, we have combined both measurements of physiological states and eCAPs with one stimulating electrode design to assess the effect caused by KES. In terms of eCAPs and KES blocking amplitude, our findings, which show the nerve conduction block starts from large myelinated fiber (A-fiber), to small myelinated (B-fiber) and unmyelinated fiber (C-fiber), is consistent with previous study in the same animal model[35,60]. Similar slowing in the conduction velocity, which is more prominent in slow fiber, was also observed in our results (Fig. 5B and Fig. S6B)[35]. Interestingly, although the eCAPs during KES demonstrate the fiber selective conduction block in sequence, the physiological states, especially HR and BI, show different trends compared to neural responses. The HR, mostly associated with B-fiber response, remains relatively unchanged across the intensity range during KES. A slight drop in HR with KES, especially at high intensity, can be explained by the activation of afferent C-fibers through a reflex mechanism, as stimulation of C-fiber has known to cause a lesser and slow-onset drop in HR compared to the greater and abrupt-onset drop with B-fiber activation[61]. The respiratory effect, mostly associated with C-fiber response, reach its maximum at the halfway of blockage in terms of eCAPs, implying that there might be asynchronous responses of C-fibers elicited by KES, but unable to be resolved by the eCAP as well the probing pulse methods. We further performed computational modeling and histological study using c-Fos^{+} to show that the KES itself, can be used to selectively excite the C-fiber and result in asynchronous APs, which cannot be assessed through probing pulses. Therefore, for the vagus nerves, potentially applying to other peripheral nerve, KES stimuli are capable of not only providing nerve conduction block, but also fiber-selective activation capability. Additionally, compared with waveform manipulation approach, the optimal intensity for KES to achieve preferential excitation is relatively stable across animals. Similar high frequency approach has also been used in deep brain stimulation and show it can target neurons in deeper layer, indicating the potential of high frequency stimulation to modulate nerve fiber in certain distance[62]. Both characteristics might make the frequency modulation more practical for clinical settings, as it has wider tolerance range with regard to the change of neural interface and variation across subjects.

Immunochemistry in Brainstem to elucidate fiber selective activation

The brainstem projections of sensory (afferent) and motor (efferent) components of the vagus nerve has been well-studied in rat. The nucleus tractus solitaries (NTS), where vagal afferent terminate, receives general visceral information from Aβ-, Aγ-, Aδ- and mostly C-fibers[63,64]. The dorsal motor vagal nucleus of vagus (DMV), where is origin of most part of vagal efferent fiber, mostly served parasympathetic vagal function in the gastrointestinal tract, lungs, other thoracic and abdominal and cardiac vagal ganglia innervations through large Aα- and B-fiber innervation[63]. Using the VNS of the right cervical branch of the vagus nerve, we activated this circuitry as evidenced by higher c-Fos activity in the ipsilateral than contralateral NTS and DMV, similar to previous studies[65]. However, the strength of c-Fos expression reflect the fact that regions of brainstem can be more selectively evoked using different stimulation protocols. As shown in Figure 7D, compared with Sham in ipsilateral regions, the percentage of increase in DMV (900%) is much greater than NTS (314%) for 30Hz VNS, as results of the deviating cluster and mean from unity line, whereas relatively smaller difference in between was observed for KHz VNS (DMV:328%, NTS: 188%). More interestingly, we found that the 30Hz VNS still induce smaller, but similar amount of change in ipsilateral DMV (188%) and NTS (131%), whereas the KHz VNS show no significant change from Sham (DMV:47%, NTS: 22%, both not significance). Results imply that the KHz VNS, compared with traditional 30Hz VNS, can be used to more preferentially activate sensory region which primarily related to C-fiber, and trigger relatively unilateral vagal activation, potentially through blocking the most of A- and B-fibers with proper intensity setting (2mA, 8-10×PT(KES)).

Computational Modeling for KES Simulation and fiber selective Mechanism

Previous nerve stimulation studies suggested the possibility of inducing selective activation in peripheral axon bundles using KES (5 ~ 50 kHz)[48]: However, precise mechanisms underlying these experimental observations are still an open question. We used biophysically-detailed computational models to explain the observed selective nerve block under different KES conditions. In order to isolate the contribution of different stimulation frequency, our computational model used sinusoid KES to ensure the identical total charge across all tested stimulation frequencies. Sinusoid and square KES have been used to induce nerve conduction blocking, and has showed similar mechanisms of blocking when the stimulus frequency was high enough [66-68]. Our simulation suggested that myelinated and unmyelinated fibers have their characteristic activation and blocking and the selectivity can be maximized by modulating the stimulus frequency. In our model, all biophysical parameters describing voltage-gated channel kinetics and ion channel distributions for different fiber types shared the same values, so the simulated fiber-specific response to KES is purely due to the different axonal size and myelin structure within the vagus nerve. Neuronal physical structure has been reported to play a vital role in shaping response properties in different nervous systems [69-71]. Our simulation indicated that functionally distinct response properties to KES can be also resulted by physical variations such as myelin structure and axonal diameter (see Fig. S9). Our model parameters were optimized based on histological information observed from functionally-identified fibers to improve the biological accuracy for cervical nerve fiber simulation. In addition, the model's predictive ability was validated by *in vivo* compound nerve action potential recordings from the same animals[46].

We noticed that our simulation is based on single fiber stimulation, while the *in vivo* results, eCAPs are obtained from a bundle of mixed fibers. Previously published literatures in VN fibers demonstrate that myelinated A-type fibers are evoked in the order Aα-type, Aβ-type, Aγ-type and Aδ-type, while our present model only included a generic A-type fiber. In future work we intend to expand our model to population-based simulation, including additional nerve fiber

types and histologically-driven fiber distribution, for more accurate VN fiber modeling. In addition, our model only included basic ionic channel and membrane properties. Newly-reported ionic currents in vagus nerves[72] and frequency-dependent membrane capacitance[48] might also influence the KES-induced selectivity. Additional *in silico* study will include nerve-specific ion channel properties to elucidate the mechanisms underlying recorded variances, as well incorporating physiologically relevant experimental designs for further model validation.

Neural and Physiological Selective Index Fiber Recruitment Calibration

In this study, we proposed a new concept of neural selective index (NSI) and physiological selective index (PSI) to optimize the desire and minimize the side effect for each stimulation protocol, and the results are consistent with each other for most of cases (Fig. 1C-D, 2C-F, 5E-F, 6C-D). Compared with the straightforward NSI, the PSI is designed for only cervical VNS, based on the established bivariate relationship and multivariate models between A-, B-, C-fiber activation and corresponding physiological marker: cervical EMG, changes in heart rate (ΔHR), and breathing interval (ΔBI)[40]. For clinical VNS therapy, optimization of parameters with respect to fiber engagement on subject basis is essential; however, registering eCAPs from the vagus nerve is not feasible in existing medical device. Therefore, the presented PSIs for different fibers, based on non-invasive measured physiological markers, can serve as an indicator of cVNS effectiveness on disease basis, for both at the time of electrode implantation and during follow up visits with health care providers. For example, the B-fiber PSI could facilitate the optimization of stimulation paradigms to treat heart failure[18] or cardiac arrhythmia[73], whereas the C-fiber PSI could act as an index of therapeutic effect in anti-inflammatory application of VNS[17].

Limitations and Future Work

The isoflurane anesthesia is commonly used in vagus and carotid sinus nerve stimulation studies[74], and is not known to alter thresholds for direct electrical activation of vagus fibers[75], nor the neural threshold in our experiment. However, we expect the detected physiological threshold used in our study will be higher as isoflurane is known to impact synaptic transmission blunt baroreflex mediated cardiac responses through downregulating synaptic transmission, though previous studies have shown that the baroreceptor-induce heart rate changes can still be observed at high isoflurane concentration[76]. Most likely, the synaptic blunting caused by isoflurane anesthesia may require activation of a larger number of parasympathetic fibers to elicit similar response, so the way we measuring PT and scaling intensity based on is still reasonable approach and physiologically meaningful.

Together with controlled neural conduction block or selective activation, the KES strategy also causes transient bi-directional neural activity[32,59]. In our study, we also found that the laryngeal muscle demonstrated strong transient response after applying KES to VN, especially intensity above blocking threshold of A- and B-fiber, which actually serves as an observable indicator for the reversible blocking effect (Fig. S6A). This transient response might also contribute to the minor c-Fos expression in ipsilateral DMV, as it evoked large myelinated fiber shortly, most likely Aα and B-fiber, before achieving complete block. The same phenomenon is also shown in our computational modeling, as transient spikes evoked just after the onset of KES (Fig. 8B, black trace, < 1ms after onset). Though the onset response might lead to side effects for clinical applications, the time window is relatively short that patients might be able to tolerate. Recent optimization method used to eliminate onset response in KES through modulating the intensity at the onset of stimuli might potentially be able to minimize the non-controllable phase[60].

The other issue related to KES is whether the it causes nerve damage and is able to generate repeatable responses, as it deposits significantly more power in tissue compared with stimulus in low frequency range. A study in spinal cord stimulation using phantom and computational model has shown that high frequency stimulus induced relative higher temperature increase over tissue than low frequency, which might alter the outcomes of KES over time[77]. In a rodent KES VNS study, it has demonstrated that the KES response, assessed with CAP recordings, is recoverable up to certain intensity level, though longer carryover durations with larger amplitude was observed[35]. Compared to their study, our KES duration is relatively short (10-s versus 25-s) while longer carryover duration (5-15-mins versus 100-s) was used for physiological response recovery. In the same rat model, both physiological and neural responses, elicited below 10×PT of KES (8-KHz, 40-μs duration, 2-2.5mA), were recoverable as consistent responses were obtained with fully randomized stimuli (Fig. S5 and S6 respectively). However, we did observe as intensity further increase, especially when C-fiber and associated breathing response disappeared gradually (30×PT of KES, 6-7.5mA), the evoked response became irreversible, as an indicator of nerve damage (data not shown). The unrecoverable stimulus parameters reported here are similar to other study[35] and this finding implies that the complete blockage of C-fiber might be challenging to achieve with high intensity KES while maintaining the integrity of vagus nerve.

In our study, we used rodent model as the recruitment of vagus nerve fibers are well-documented and in fact have been used to define the classification of different fiber types based on their conduction velocity and anatomical characteristics[78]. In addition, rodent models are ideal to study stimulus protocols specific to each type of VN fibers, as fascicular structure has been greatly simplified from many (5-10 in human and 20-50 in swine) to few (1-2 in rodent), while the characteristics of each fiber type remain similar. However, to translate those findings to the large animal model or human, the identified stimulation strategies need to be retested, as the distance between electrode to the fiber of interest increases and spans a larger range in the complex, multi-fascicle, large diameter nerves[75]. Special designs of electrode, such as multi-contacts[79], inter-fascicular, or intra-fascicular electrode[80] might provide further spatial selectivity and result in similar fiber selective capability within target fascicle.

Author contributions

YCC conceived and designed experiments, performed experiments, analyzed and interpreted experimental results, and wrote/reviewed the paper. UA conceived and performed rat experiments. NJ and YCW designed and performed immunohistology experiments. AA and IM designed and performed mouse experiment. QL, TG, and SD designed and performed the computational stimulation, and wrote the paper. AG performed rat experiments. AD and JA performed the histological analysis. SD and YAA critically reviewed the paper. SZ conceived and designed experiments, analyzed and interpreted experimental results, and wrote/reviewed the paper.

Declaration of interests

The research was partially supported by a grant to SZ from United Therapeutics Corporation (MD, US). SZ and YCC have a provisional patent application with United Therapeutics Corporation that includes aspects of the research presented in this paper. The other authors declare no conflict of interest.

Data and materials availability: The data that support the findings of this study are available from the corresponding author upon reasonable request.

References

1 Johnson, R. L. & Wilson, C. G. A review of vagus nerve stimulation as a therapeutic intervention. *Journal of inflammation research* **11**, 203-213, doi:10.2147/JIR.S163248 (2018).

2 Pratap, R., Farboud, A., Patel, H. & Montgomery, P. Vagal nerve stimulator implantation: the otolaryngologist's perspective. *European archives of oto-rhino-laryngology : official journal of the European Federation of Oto-Rhino-Laryngological Societies* **266**, 1455-1459, doi:10.1007/s00405-008-0887-2 (2009).

3 Ben-Menachem, E. Vagus-nerve stimulation for the treatment of epilepsy. *The Lancet. Neurology* **1**, 477-482 (2002).

4 Sackeim, H. A. *et al.* Vagus nerve stimulation (VNS) for treatment-resistant depression: efficacy, side effects, and predictors of outcome. *Neuropsychopharmacology : official publication of the American College of Neuropsychopharmacology* **25**, 713-728, doi:10.1016/S0893-133X(01)00271-8 (2001).

5 Koopman, F. A. *et al.* Vagus nerve stimulation inhibits cytokine production and attenuates disease severity in rheumatoid arthritis. *Proceedings of the National Academy of Sciences of the United States of America* **113**, 8284-8289, doi:10.1073/pnas.1605635113 (2016).

6 Merrill, C. A. *et al.* Vagus nerve stimulation in patients with Alzheimer's disease: Additional follow-up results of a pilot study through 1 year. *The Journal of clinical psychiatry* **67**, 1171-1178 (2006).

7 Chakravarthy, K., Chaudhry, H., Williams, K. & Christo, P. J. Review of the Uses of Vagal Nerve Stimulation in Chronic Pain Management. *Current pain and headache reports* **19**, 54, doi:10.1007/s11916-015-0528-6 (2015).

8 George, M. S. *et al.* A pilot study of vagus nerve stimulation (VNS) for treatment-resistant anxiety disorders. *Brain stimulation* **1**, 112-121, doi:10.1016/j.brs.2008.02.001 (2008).

9 Tyler, R. *et al.* Vagus Nerve Stimulation Paired with Tones for the Treatment of Tinnitus: A Prospective Randomized Double-blind Controlled Pilot Study in Humans. *Scientific reports* **7**, 11960, doi:10.1038/s41598-017-12178-w (2017).

10 De Ferrari, G. M. *et al.* Long-term vagal stimulation for heart failure: Eighteen month results from the NEural Cardiac TherApy foR Heart Failure (NECTAR-HF) trial. *International journal of cardiology* **244**, 229-234, doi:10.1016/j.ijcard.2017.06.036 (2017).

11 Meyers, E. E., Kronemberger, A., Lira, V., Rahmouni, K. & Stauss, H. M. Contrasting effects of afferent and efferent vagal nerve stimulation on insulin secretion and blood glucose regulation. *Physiological reports* **4**, doi:10.14814/phy2.12718 (2016).

12 Pardo, J. V. *et al.* Weight loss during chronic, cervical vagus nerve stimulation in depressed patients with obesity: an observation. *International journal of obesity* **31**, 1756-1759, doi:10.1038/sj.ijo.0803666 (2007).

13 Yoshida, K. *et al.* Electrical Vagal Nerve Stimulation Ameliorates Pulmonary Vascular Remodeling and Improves Survival in Rats With Severe Pulmonary Arterial Hypertension. *JACC. Basic to translational science* **3**, 657-671, doi:10.1016/j.jacbts.2018.07.007 (2018).

14 Bao, M., Zhou, J. & Luan, G. M. Treatment of drug-resistant epilepsy with vagus nerve stimulation -- review of 45 cases. *Chinese medical journal* **124**, 4184-4188 (2011).

15 Yoo, P. B. *et al.* High-resolution measurement of electrically-evoked vagus nerve activity in the anesthetized dog. *Journal of neural engineering* **10**, 026003, doi:10.1088/1741-2560/10/2/026003 (2013).

16 Olofsson, P. S. *et al.* Single-Pulse and Unidirectional Electrical Activation of the Cervical Vagus Nerve Reduces Tumor Necrosis Factor in Endotoxemia. *Bioelectronic Medicine* **2**, 37-42, doi:10.15424/bioelectronmed.2015.00006 (2015).

17 Sundman, E. & Olofsson, P. S. Neural control of the immune system. *Advances in physiology education* **38**, 135-139, doi:10.1152/advan.00094.2013 (2014).

18 Gold, M. R. *et al.* Vagus Nerve Stimulation for the Treatment of Heart Failure: The INOVATE-HF Trial. *Journal of the American College of Cardiology* **68**, 149-158, doi:10.1016/j.jacc.2016.03.525 (2016).
19 De Ferrari, G. M. *et al.* Chronic vagus nerve stimulation: a new and promising therapeutic approach for chronic heart failure. *European heart journal* **32**, 847-855, doi:10.1093/eurheartj/ehq391 (2011).
20 Zannad, F. *et al.* Chronic vagal stimulation for the treatment of low ejection fraction heart failure: results of the NEural Cardiac TherApy foR Heart Failure (NECTAR-HF) randomized controlled trial. *European heart journal* **36**, 425-433, doi:10.1093/eurheartj/ehu345 (2015).
21 Premchand, R. K. *et al.* Autonomic regulation therapy via left or right cervical vagus nerve stimulation in patients with chronic heart failure: results of the ANTHEM-HF trial. *Journal of cardiac failure* **20**, 808-816, doi:10.1016/j.cardfail.2014.08.009 (2014).
22 Vuckovic, A., Tosato, M. & Struijk, J. J. A comparative study of three techniques for diameter selective fiber activation in the vagal nerve: anodal block, depolarizing prepulses and slowly rising pulses. *Journal of neural engineering* **5**, 275-286, doi:10.1088/1741-2560/5/3/002 (2008).
23 Ahmed, U. *et al.* Anodal block permits directional vagus nerve stimulation. *Scientific reports* **10**, 9221, doi:10.1038/s41598-020-66332-y (2020).
24 Jones, J. F., Wang, Y. & Jordan, D. Heart rate responses to selective stimulation of cardiac vagal C fibres in anaesthetized cats, rats and rabbits. *The Journal of physiology* **489 (Pt 1)**, 203-214, doi:10.1113/jphysiol.1995.sp021042 (1995).
25 Hennings, K., Arendt-Nielsen, L. & Andersen, O. K. Orderly activation of human motor neurons using electrical ramp prepulses. *Clinical Neurophysiology* **116**, 597-604, doi:https://doi.org/10.1016/j.clinph.2004.09.011 (2005).
26 Tosato, M., Yoshida, K., Toft, E. & Struijk, J. J. Quasi-trapezoidal pulses to selectively block the activation of intrinsic laryngeal muscles during vagal nerve stimulation. *Journal of neural engineering* **4**, 205-212, doi:10.1088/1741-2560/4/3/005 (2007).
27 Hennings, K., Arendt-Nielsen, L., Christensen, S. S. & Andersen, O. K. Selective activation of small-diameter motor fibres using exponentially rising waveforms: A theoretical study. *Medical and Biological Engineering and Computing* **43**, 493-500, doi:10.1007/BF02344731 (2005).
28 Grill, W. M. & Mortimer, J. T. Stimulus waveforms for selective neural stimulation. *IEEE Engineering in Medicine and Biology Magazine* **14**, 375-385, doi:10.1109/51.395310 (1995).
29 Grill, W. M. & Mortimer, J. T. Inversion of the current-distance relationship by transient depolarization. *IEEE Transactions on Biomedical Engineering* **44**, 1-9, doi:10.1109/10.553708 (1997).
30 Fang, Z. P. & Mortimer, J. T. Selective activation of small motor axons by quasi-trapezoidal current pulses. *IEEE transactions on bio-medical engineering* **38**, 168-174, doi:10.1109/10.76383 (1991).
31 Bhadra, N. & Mortimer, J. T. Selective block of external anal sphincter activation during electrical stimulation of the sacral anterior roots in a canine model. *Neurogastroenterology and motility : the official journal of the European Gastrointestinal Motility Society* **17**, 721-726, doi:10.1111/j.1365-2982.2005.00678.x (2005).
32 Kilgore, K. L. & Bhadra, N. Reversible nerve conduction block using kilohertz frequency alternating current. *Neuromodulation : journal of the International Neuromodulation Society* **17**, 242-255, doi:10.1111/ner.12100 (2014).
33 Apovian, C. M. *et al.* Two-Year Outcomes of Vagal Nerve Blocking (vBloc) for the Treatment of Obesity in the ReCharge Trial. *Obesity surgery* **27**, 169-176, doi:10.1007/s11695-016-2325-7 (2017).
34 Johannessen, H. *et al.* Vagal Blocking for Obesity Control: a Possible Mechanism-Of-Action. *Obesity surgery* **27**, 177-185, doi:10.1007/s11695-016-2278-x (2017).

35 Pelot, N. A. & Grill, W. M. In vivo quantification of excitation and kilohertz frequency block of the rat vagus nerve. *Journal of neural engineering* **17**, 026005, doi:10.1088/1741-2552/ab6cb6 (2020).
36 Zhao, Y. *et al.* Neuromuscular Electrical Stimulation with Kilohertz Frequency Alternating Current to Enhance Sensorimotor Cortical Excitability. *Conference proceedings : ... Annual International Conference of the IEEE Engineering in Medicine and Biology Society. IEEE Engineering in Medicine and Biology Society. Annual Conference* **2018**, 2240-2243, doi:10.1109/EMBC.2018.8512855 (2018).
37 Negi, S., Bhandari, R., Rieth, L. & Solzbacher, F. In vitro comparison of sputtered iridium oxide and platinum-coated neural implantable microelectrode arrays. *Biomedical materials* **5**, 15007, doi:10.1088/1748-6041/5/1/015007 (2010).
38 Negi, S., Bhandari, R., Rieth, L., Van Wagenen, R. & Solzbacher, F. Neural electrode degradation from continuous electrical stimulation: comparison of sputtered and activated iridium oxide. *Journal of neuroscience methods* **186**, 8-17, doi:10.1016/j.jneumeth.2009.10.016 (2010).
39 Levy, T. J. *et al.* An impedance matching algorithm for common-mode interference removal in vagus nerve recordings. *Journal of neuroscience methods* **330**, 108467, doi:10.1016/j.jneumeth.2019.108467 (2019).
40 Chang, Y. C. *et al.* Quantitative estimation of nerve fiber engagement by vagus nerve stimulation using physiological markers. *Brain stimulation* **13**, 1617-1630, doi:10.1016/j.brs.2020.09.002 (2020).
41 Chang, Y. *et al.* in *2019 41st Annual International Conference of the IEEE Engineering in Medicine and Biology Society (EMBC).* 6278-6281.
42 L Parker, J., H Shariati, N. & M Karantonis, D. Electrically evoked compound action potential recording in peripheral nerves. *Bioelectronics in medicine* **1**, 71-83, doi:10.2217/bem-2017-0005 (2018).
43 McIntyre, C. C., Richardson, A. G. & Grill, W. M. Modeling the excitability of mammalian nerve fibers: influence of afterpotentials on the recovery cycle. *Journal of neurophysiology* **87**, 995-1006, doi:10.1152/jn.00353.2001 (2002).
44 Schwarz, J. R., Reid, G. & Bostock, H. Action-potentials and membrane currents in the human node of ranvier. *Eur J Phy* **430**, 283-292, doi:Doi 10.1007/Bf00374660 (1995).
45 Dokos, S. *Modelling Organs, Tissues, Cells and Devices Using MATLAB and COMSOL Multiphysics*. (Springer 2017).
46 Lin, Q. *et al.* A Computational Model of Functionally-distinct Cervical Vagus Nerve Fibers. *Annual International Conference of the IEEE Engineering in Medicine and Biology Society. IEEE Engineering in Medicine and Biology Society. Annual International Conference* **2020**, 2475-2478, doi:10.1109/EMBC44109.2020.9175855 (2020).
47 Guo, T. *et al.* Mediating Retinal Ganglion Cell Spike Rates Using High-Frequency Electrical Stimulation. *Frontiers in neuroscience* **13**, doi:10.3389/fnins.2019.00413 (2019).
48 Joseph, L. & Butera, R. J. High-frequency stimulation selectively blocks different types of fibers in frog sciatic nerve. *IEEE transactions on neural systems and rehabilitation engineering : a publication of the IEEE Engineering in Medicine and Biology Society* **19**, 550-557, doi:10.1109/TNSRE.2011.2163082 (2011).
49 Kameneva, T. *et al.* Retinal ganglion cells: mechanisms underlying depolarization block and differential responses to high frequency electrical stimulation of ON and OFF cells. *Journal of neural engineering* **13**, 016017, doi:10.1088/1741-2560/13/1/016017 (2016).
50 Kilgore, K. L. & Bhadra, N. Nerve conduction block utilising high-frequency alternating current. *Medical & biological engineering & computing* **42**, 394-406, doi:10.1007/BF02344716 (2004).

51 Krahl, S. E., Senanayake, S. S. & Handforth, A. Destruction of peripheral C-fibers does not alter subsequent vagus nerve stimulation-induced seizure suppression in rats. *Epilepsia* **42**, 586-589, doi:10.1046/j.1528-1157.2001.09700.x (2001).
52 Banzett, R. B. *et al.* Cardiorespiratory variables and sensation during stimulation of the left vagus in patients with epilepsy. *Epilepsy research* **35**, 1-11, doi:10.1016/s0920-1211(98)00126-0 (1999).
53 Mughrabi, I. T. *et al.* An implant for long-term cervical vagus nerve stimulation in mice. *bioRxiv*, 2020.2006.2020.160473, doi:10.1101/2020.06.20.160473 (2020).
54 Bhadra, N. & Kilgore, K. L. Direct current electrical conduction block of peripheral nerve. *IEEE transactions on neural systems and rehabilitation engineering : a publication of the IEEE Engineering in Medicine and Biology Society* **12**, 313-324, doi:10.1109/TNSRE.2004.834205 (2004).
55 Patel, Y. A., Kim, B. S., Rountree, W. S. & Butera, R. J. Kilohertz Electrical Stimulation Nerve Conduction Block: Effects of Electrode Surface Area. *IEEE transactions on neural systems and rehabilitation engineering : a publication of the IEEE Engineering in Medicine and Biology Society* **25**, 1906-1916, doi:10.1109/TNSRE.2017.2684161 (2017).
56 Buckley, U. *et al.* Bioelectronic neuromodulation of the paravertebral cardiac efferent sympathetic outflow and its effect on ventricular electrical indices. *Heart rhythm* **14**, 1063-1070, doi:10.1016/j.hrthm.2017.02.020 (2017).
57 Patel, Y. A., Saxena, T., Bellamkonda, R. V. & Butera, R. J. Kilohertz frequency nerve block enhances anti-inflammatory effects of vagus nerve stimulation. *Scientific reports* **7**, 39810, doi:10.1038/srep39810 (2017).
58 Patel, Y. A. & Butera, R. J. Differential fiber-specific block of nerve conduction in mammalian peripheral nerves using kilohertz electrical stimulation. *Journal of neurophysiology* **113**, 3923-3929, doi:10.1152/jn.00529.2014 (2015).
59 Patel, Y. A. & Butera, R. J. Challenges associated with nerve conduction block using kilohertz electrical stimulation. *Journal of neural engineering* **15**, 031002, doi:10.1088/1741-2552/aaadc0 (2018).
60 Yi, G. & Grill, W. M. Kilohertz waveforms optimized to produce closed-state Na+ channel inactivation eliminate onset response in nerve conduction block. *PLoS computational biology* **16**, e1007766, doi:10.1371/journal.pcbi.1007766 (2020).
61 McAllen, R. M., Shafton, A. D., Bratton, B. O., Trevaks, D. & Furness, J. B. Calibration of thresholds for functional engagement of vagal A, B and C fiber groups in vivo. *Bioelectronics in medicine* **1**, 21-27, doi:10.2217/bem-2017-0001 (2018).
62 Grossman, N. *et al.* Noninvasive Deep Brain Stimulation via Temporally Interfering Electric Fields. *Cell* **169**, 1029-1041 e1016, doi:10.1016/j.cell.2017.05.024 (2017).
63 Berthoud, H. R. & Neuhuber, W. L. Functional and chemical anatomy of the afferent vagal system. *Autonomic neuroscience : basic & clinical* **85**, 1-17, doi:10.1016/S1566-0702(00)00215-0 (2000).
64 Beaumont, E. *et al.* Cervical vagus nerve stimulation augments spontaneous discharge in second- and higher-order sensory neurons in the rat nucleus of the solitary tract. *American journal of physiology. Heart and circulatory physiology* **313**, H354-H367, doi:10.1152/ajpheart.00070.2017 (2017).
65 Huffman, W. J. *et al.* Modulation of neuroinflammation and memory dysfunction using percutaneous vagus nerve stimulation in mice. *Brain stimulation* **12**, 19-29, doi:10.1016/j.brs.2018.10.005 (2019).
66 Zhang, X., Roppolo, J. R., de Groat, W. C. & Tai, C. Mechanism of nerve conduction block induced by high-frequency biphasic electrical currents. *IEEE transactions on bio-medical engineering* **53**, 2445-2454, doi:10.1109/TBME.2006.884640 (2006).

67 Bhadra, N., Lahowetz, E. A., Foldes, S. T. & Kilgore, K. L. Simulation of high-frequency sinusoidal electrical block of mammalian myelinated axons. *Journal of computational neuroscience* **22**, 313-326, doi:10.1007/s10827-006-0015-5 (2007).
68 Tai, C. F., de Groat, W. C. & Roppolo, J. R. Simulation analysis of conduction block in unmyelinated axons induced by high-frequency biphasic electrical currents. *Ieee Transactions on Biomedical Engineering* **52**, 1323-1332, doi:10.1109/Tbme.2005.847561 (2005).
69 Vetter, P., Roth, A. & Hausser, M. Propagation of action potentials in dendrites depends on dendritic morphology. *Journal of neurophysiology* **85**, 926-937 (2001).
70 Spruston, N. Pyramidal neurons: dendritic structure and synaptic integration. *Nature reviews. Neuroscience* **9**, 206-221, doi:10.1038/nrn2286 (2008).
71 Wang, J., Jacoby, R. & Wu, S. M. Physiological and morphological characterization of ganglion cells in the salamander retina. *Vision Res* **119**, 60-72, doi:10.1016/j.visres.2015.12.007 (2016).
72 Pelot, N. A. *et al.* Excitation properties of computational models of unmyelinated peripheral axons. *Journal of neurophysiology* **125**, 86-104, doi:10.1152/jn.00315.2020 (2021).
73 Nasi-Er, B. G. *et al.* Vagus nerve stimulation reduces ventricular arrhythmias and increases ventricular electrical stability. *Pacing and clinical electrophysiology : PACE* **42**, 247-256, doi:10.1111/pace.13585 (2019).
74 Thompson, G. W. *et al.* Bradycardia induced by intravascular versus direct stimulation of the vagus nerve. *The Annals of thoracic surgery* **65**, 637-642, doi:10.1016/s0003-4975(97)01351-9 (1998).
75 Nicolai, E. N. *et al.* Sources of off-target effects of vagus nerve stimulation using the helical clinical lead in domestic pigs. *Journal of neural engineering* **17**, 046017, doi:10.1088/1741-2552/ab9db8 (2020).
76 Bagshaw, R. J. & Cox, R. H. Baroreceptor control of central and regional hemodynamics with isoflurane in the dog. *Acta anaesthesiologica Scandinavica* **32**, 82-92, doi:10.1111/j.1399-6576.1988.tb02693.x (1988).
77 Zannou, A. L. *et al.* Temperature increases by kilohertz frequency spinal cord stimulation. *Brain stimulation* **12**, 62-72, doi:10.1016/j.brs.2018.10.007 (2019).
78 Woodbury, D. M. & Woodbury, J. W. Effects of vagal stimulation on experimentally induced seizures in rats. *Epilepsia* **31 Suppl 2**, S7-19, doi:10.1111/j.1528-1157.1990.tb05852.x (1990).
79 Aristovich, K. *et al.* Model-based geometrical optimisation and in vivo validation of a spatially selective multielectrode cuff array for vagus nerve neuromodulation. *arXiv:1903.12459 [physics]* (2020).
80 Larson, C. E. & Meng, E. A review for the peripheral nerve interface designer. *Journal of neuroscience methods* **332**, 108523, doi:10.1016/j.jneumeth.2019.108523 (2020).